

# Simplified method for performance-based seismic design of suction caissons supporting jacket offshore wind turbines

**Journal Article****Author(s):**

Antoniou, Maria; Kourkoulis, Rallis; Gelagoti, Fani; Anastasopoulos, Ioannis

**Publication date:**

2022-04

**Permanent link:**

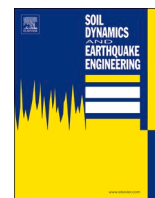
<https://doi.org/10.3929/ethz-b-000533360>

**Rights / license:**

[Creative Commons Attribution-NonCommercial-NoDerivatives 4.0 International](#)

**Originally published in:**

Soil Dynamics and Earthquake Engineering 155, <https://doi.org/10.1016/j.soildyn.2022.107169>



# Simplified method for performance-based seismic design of suction caissons supporting jacket offshore wind turbines

M. Antoniou<sup>a</sup>, R. Kourkoulis<sup>b</sup>, F. Gelagoti<sup>c</sup>, I. Anastasopoulos<sup>a,\*</sup>

<sup>a</sup> Chair of Geotechnical Engineering, ETH Zurich, Switzerland

<sup>b</sup> National Technical University of Athens, Greece

<sup>c</sup> Grid Engineers, Greece

## ARTICLE INFO

### Keywords:

Suction caissons  
Jacket structure  
FE modelling  
Winkler-based models  
Dimensional analysis  
Earthquake

## ABSTRACT

The paper studies the performance of Offshore Wind Turbines (OWTs) founded on Suction Bucket Jackets (SBJs) in clay under combined wind and seismic loading. A detailed 3D FE model of the soil–foundation–structure (SFS) system is developed and used as a *benchmark* to assess the efficiency of an enhanced Winkler-based "Caisson-on-Winkler-Soil" (CWS) model, where the soil is replaced by nonlinear hysteretic elements. The proposed CWS model captures residual deformations and hysteresis and offers physical coupling between vertical and moment loading. It allows excellent prediction of the  $H$ – $M$  failure envelope in the most relevant first quadrant of  $H$ – $M$  space, where the loads act in the same direction. Despite its successful application for the simulation of inertial loading, the CWS model fails to reproduce the *dual shearing* mechanism that develops at the caisson shaft during shaking, stemming from the combination of *kinematic* soil shearing due to the vertically propagating shear waves, and shearing due to the superstructure *inertial* response, thus underpredicting the co-seismic caisson settlements. For the prediction of the latter, the research utilizes spectrum compatible input motions and 3D FE models of varying geometric and material properties to derive linear regression equations that correlate the co-seismic dimensionless settlement of caissons ( $w_E/D$ ) with characteristic dimensional variables of the problem under investigation and the Arias Intensity ( $I_A$ ) of the surface ground motion. As a final step, the paper proposes a hybrid method for performance-based assessment of SBJ OWTs. The proposed method employs the simplified CWS model to calculate the VHM loads and approximately estimate horizontal displacements and rotations at the jacket legs, followed by a preliminary assessment of caisson settlements using the correlations of  $w_E/D$  with  $I_A$ , on the basis of spectrum-compatible input motions.

## 1. Introduction

Following the ambitious energy targets set by countries worldwide, the offshore wind sector has seen impressive growth over the last decade, transforming from niche technology to a global industry. As of 2019, Europe alone has 22 GW of installed offshore wind capacity – enough to cover 2.3% of its electricity consumption [1], while similar or even more potent growth is observed in many countries around the world, such as China, the USA, and India. Part of this energy transition is led by technology-driven innovation, with offshore wind turbines reaching new heights and larger capacities, while wind farms are moving deeper into the sea to harness the increased energy potential. Given this new "deep-water" environment, traditional OWT support structures are gradually being replaced by more cost-effective and agile

foundation systems in a quest for reduction of investment costs.

Despite their obvious attractiveness, floating concepts require further development before commercialisation. Thanks to substantial progress towards standardized manufacturing and mass production of tubular joints using automatic welding, jackets are gradually establishing their position in the offshore industry [2–4]. They are currently the second most installed OWT foundation in Europe. Suction caissons (or buckets) were recently deployed as the foundation of jacket OWTs, including installations at the Borkum Riffgrund 1 (2014), Borkum Riffgrund 2 (2018), and Aberdeen Bay (2018) offshore windfarms. Suction caissons are decisively entering the market; their cost-efficient and low-noise installation (facilitated by water pumping between the caisson and the soil, with the hydraulic pressure difference driving the caisson into the soil) offers a major comparative advantage.

At the same time, the spread of such installations has broadened the

\* Corresponding author.

E-mail address: [ixa@ethz.ch](mailto:ixa@ethz.ch) (I. Anastasopoulos).

<https://doi.org/10.1016/j.soildyn.2022.107169>

Received 21 May 2021; Received in revised form 27 December 2021; Accepted 21 January 2022

Available online 7 February 2022

0267-7261/© 2022 The Authors.

Published by Elsevier Ltd.

This is an open access article under the CC BY-NC-ND license

(<http://creativecommons.org/licenses/by-nc-nd/4.0/>).

Notations	
$a$	Acceleration
$a_{tower}$	Acceleration at the turbine tower top
$a_{surface}$	Acceleration at the soil surface
$A$	Area
$A_r$	Arias Intensity ratio
$B$	Jacket width
$C_{dash}$	Dashpot coefficient
$C$	Initial modulus of the kinematic hardening constitutive model
$D$	Caisson diameter
$D_{tower}$	Diameter of the turbine tower
$d_{rotor}$	Rotor diameter
$E$	Earthquake load
$E_{o,ns}$	Small-strain stiffness of hysteretic elements
$E_o$	Small-strain soil stiffness
$E_{steel}$	Young's modulus of steel
$E_{ur, ns}$	Unloading/Reloading modulus of hysteretic elements
$F$	Yield surface of the kinematic hardening constitutive model
$f_E$	Predominant seismic frequency
$f_{cyc}$	Cyclic force
$f_{max}$	Ultimate strength of hysteretic elements
$f_{yield}$	Steel yield stress
$G$	Soil shear modulus
$H$	Horizontal load
$H_b$	Horizontal resistance at the caisson base
$H_o$	Pure horizontal caisson capacity
$H_{shaft}$	Horizontal resistance at the caisson shaft
$H_{shaft,n}$	Horizontal shear traction on the caisson sides parallel to the loading direction
$H_{shaft,s}$	Passive & active reaction on the caisson sides perpendicular to the loading direction
$H_{tower}$	Height of the turbine tower
$I_A$	Arias' Intensity
$J$	Relative soil-caisson rigidity ratio
$k_e$	Uniaxial elastic stiffness of hysteretic elements
$k_{x,n}$	Distributed normal horizontal stiffness
$k_{x,s}$	Distributed frictional horizontal stiffness
$k_z$	Distributed shaft vertical stiffness
$K_{HH}$	Caisson lateral stiffness
$K_{MH}$	Caisson coupled swaying-rocking stiffness
$K_{MM}$	Caisson rocking stiffness
$K_{b\theta}$	Rotational stiffness of the caisson base
$K_{bx}$	Lateral stiffness of the caisson base
$K_{bz}$	Vertical stiffness of the caisson base
$L$	Length
$M$	Moment load
$M_b$	Moment resistance of caisson base
$M_{shaft}$	Moment resistance of caisson shaft
$M_{shaft,y}$	Shaft resisting moment generated by vertical shear stresses on the shaft
$M_{shaft,x}$	Shaft resisting moment generated by horizontal stresses
$M_o$	Pure moment caisson capacity
$N_{cH}$	Uniaxial horizontal capacity factor
$N_{cH, base}$	Local horizontal capacity factor at the caisson base
$N_{cH, shaft}$	Local horizontal capacity factor at the caisson shaft
$N_{cM}$	Uniaxial moment capacity factor
$N_{cM, base}$	Local moment capacity factor at the caisson base
$N_{cM, shaft}$	Local moment capacity factors at the caisson shaft
$N_{cV}$	Uniaxial vertical capacity factor
$N_{cV, base}$	Local vertical capacity factor at the caisson base
$N_{cV, shaft}$	Local vertical capacity factor at the caisson shaft
$PGA$	Peak ground acceleration
$PI$	Clay plasticity index
$RSD$	Relative significant duration
$S_u$	Undrained shear strength
$t_{tower}$	Thickness of the turbine tower
$t_w$	Caisson skirt thickness
$T_{1,n}$	First natural period of the OWT system
$T_E$	Predominant earthquake period
$u$	Horizontal caisson displacement
$V$	Vertical load
$V_b$	Vertical resistance of caisson base
$V_o$	Pure vertical caisson capacity
$V_s$	Shear wave velocity
$V_{shaft}$	Vertical resistance of caisson shaft
$V_w$	Static vertical load on the windward caisson leg, corresponding to dead loads & wind load
$W$	Wind load
$W_{SLS}$	Wind load at SLS conditions
$w$	Vertical caisson displacement
$w_c$	Vertical displacement of the compressive (windward) jacket leg
$w_t$	Vertical displacement of the tensile (leeward) jacket leg
$x$	Horizontal in-plane direction
$y$	Horizontal out-of-plane direction
$z$	Vertical direction
$a_0$	Dimensionless frequency
$\alpha$	Backstress tensor in the kinematic hardening constitutive model
$\beta$	Scalar coefficient of the linear regression equations
$\gamma$	Scalar coefficient of the kinematic hardening constitutive model
$\gamma_{xz}$	Shear strain in the x – z plane
$\gamma_V$	Shear strain due to vertical loading
$\gamma_E$	Shear strain due to seismic loading
$\delta$	Scalar coefficient of the linear regression equations
$\Delta(\omega)$	Dynamic stiffness coefficient
$\theta$	Caisson rotation
$\Theta_j$	Rotation of the jacket structure
$\nu$	Poisson's ratio
$\rho$	Material density
$\sigma_{Mises}$	Mises stress
$\sigma_y$	Maximum yield stress at saturation
$\sigma_o$	Maximum stress at zero plastic strain
$\tau_{xz}$	Shear stress in the x – z plane
$\omega$	Angular frequency
$\dot{\alpha}$	Evolution law of the backstress tensor $\alpha$
$\underline{s}$	Deviatoric stress tensor of the kinematic hardening constitutive model

hazard spectrum faced by OWTs [5–7]. In recent years, a large number of wind turbines have been installed (or are planned to be installed) in high-seismicity areas, including China, Taiwan, India, and South Korea, as well as the USA, Mexico, and several seismically active zones in Southern Europe and the Middle East. According to Swiss Re [6], a

50-year seismic event could trigger losses of millions of USD in vulnerable offshore wind markets by 2030 (DNV, ACE Project). Amid persisting concerns on the structural robustness of OWTs in earthquake-prone

areas, DNV GL recently launched the ACE (Alleviating Cyclone and Earthquake Challenges for Wind farms) Joint Industry Project.<sup>1</sup>

Despite the growing literature on the seismic performance of OWTs [8–12], several crucial issues remain. For example, the coupling of aerodynamic, hydrodynamic, and seismic loading was only recently explored for fixed-base OWTs (numerically and experimentally), confirming the non-trivial effect of tower seismic oscillation on rotor aerodynamics and the developing wind thrust [13–15]. The effects of the combined action of wind and earthquake loading have been discussed in Gelagoti et al. [16] focusing on foundation performance. The study analyzed a 10 MW OWT, supported on a large diameter monopile and a 4-legged jacket founded on piles. They observed a considerable accumulation of permanent deformations for both foundation systems when subjected to large-amplitude non-symmetric cyclic loading (due to the combined action of wind and seismic loading).

Significant research effort has been devoted to the response of suction caisson as an alternative foundation for OWTs, with the vast majority of the literature focusing on monopod installations [17–24]. To the best of our knowledge, only limited studies have addressed the dynamic performance of suction caissons. Suryasentana et al. [25] presented an elastoplastic 1D Winkler-based model for suction caissons under VHM loading. By combining Winkler-type elastic soil reactions with local plastic yield surfaces, the model captured the monotonic and symmetric cyclic foundation response. A macro-element approach was proposed by Skau et al. [26,27] to capture the nonlinear behaviour of flexible or rigid suction caissons in clay under irregular cyclic loading. Wang et al. [28] analyzed the lateral seismic response of monopod suction buckets in sand through centrifuge model testing. Esfeh & Kaynia [73] investigated numerically the effect of liquefaction on the performance of monopod caisson foundations in sand under the combined actions of ground shaking and static/cyclic wind loading. Employing 3D finite element (FE) modelling, Kourkoulis et al. [74] evaluated the effect of soil-sidewall interfaces on the response of wind turbines founded on monopod suction caissons in clay under lateral monotonic, cyclic and seismic loading.

Despite the recent advances and the valuable insights offered by sophisticated numerical and physical models, practice calls for efficient performance-based design techniques. To this end, this paper develops a simplified performance-based methodology for OWTs founded on Suction Bucket Jackets (SBJ) in clay, subjected to combined environmental and seismic loading. An enhanced Winkler-based "Caisson-on-Winkler-Soil" (CWS) model is developed for this purpose, where soil-suction caisson interaction is represented by nonlinear hysteretic elements allowing the simulation of residual deformations. Moreover, the proposed CWS model captures the coupling between vertical and moment loading, using distributed vertical hysteretic elements on the caisson shaft, which contribute simultaneously to the axial and moment shaft resistance under combined VHM loading. A detailed 3D FE model of the entire soil–foundation–structure (SFS) system is developed and used as a benchmark to assess the efficiency of the simplified analysis technique.

While the detailed 3D FE model is certainly more robust, the unavoidably less precise simplified CWS model offers the advantage of computational efficiency. The two modelling approaches are comparatively discussed to: (a) understand the mechanics governing the nonlinear deformation (displacement, rotation, settlement) of suction caissons under combined wind and earthquake loading; (b) explore the limitations of the CWS model; and (c) develop a simplified hybrid methodology to facilitate a performance-based assessment of the foundation of SBJ OWTs. The latter combines the CWS model for estimation of VHM loads and horizontal displacements/rotations at the jacket legs with a regression model for the assessment of settlements (based on 3D FE analyses).

<sup>1</sup> <https://www.dnvgl.com/article/alleviating-cyclone-and-earthquake-challenges-for-wind-farms-174635>.

## 2. Detailed 3D FE modelling

This section presents the detailed 3D FE modelling of the entire soil–foundation–structure (SFS) system, which is used as a benchmark to assess the efficiency of the simplified CWS model. Before diving into the full SFS system of the SBJ OWT, the numerical modelling of a single suction caisson is discussed in detail.

### 2.1. Single suction caisson

A single suction caisson of length to diameter ratio  $L/D = 1$  is analyzed, embedded in a uniform clay stratum. The problem is solved numerically, employing 3D FE modelling using ABAQUS [75]. As shown in the FE mesh of Fig. 1a, half of the caisson is modelled, taking advantage of problem symmetry. Model boundaries are at a sufficiently large distance to avoid boundary effects:  $2.5D$  at either side of the foundation for the lateral boundaries, and  $1.5L$  beneath its tip for the bottom boundary. For static loading, the lateral displacements ( $x$  and  $y$ ) are restrained at the lateral model boundaries, as well as the out-of-plane displacement ( $y$ ) for the planes of symmetry and the vertical displacement ( $z$ ) at the model base.

The steel suction caisson is simulated with linear shell elements (S4) of Young's modulus  $E_{steel} = 210$  GPa, Poisson's ratio  $\nu = 0.2$ , and density  $\rho = 7.85$  t/m<sup>3</sup>, while the soil is modelled as a one-phase medium of uniform undrained shear strength ( $S_u$ ) described by 8-noded hexahedral continuum elements (C3D8). Rough interface conditions (no separation or detachment) are assumed between the soil and the caisson. The nonlinear hysteretic behavior of clay under undrained conditions is modelled with a kinematic hardening constitutive model with Von Mises failure criterion. Gerolymos & Gazetas [29] and Anastasopoulos et al. [30] provide more details on the model and its calibration. Herein, it is briefly described for completeness. The yield surface is defined by:

$$F = f(\underline{s} - \underline{a}) - \sigma_o = 0 \quad (1)$$

where:  $\sigma_o$  corresponds to the maximum stress at zero plastic strain and  $f(\underline{s} - \underline{a})$  is the equivalent Mises stress with respect to the deviatoric stress  $\underline{s}$  and the backstress  $\underline{a}$ . The center of the yield surface is determined by the evolution law:

$$\dot{\underline{a}} = C \frac{1}{\sigma_o} \left( \underline{s} - \underline{a} \right) \frac{dP}{\epsilon} - \gamma \alpha \frac{dP}{\epsilon} \quad (2)$$

In Eq. (2),  $C$  is the initial kinematic hardening modulus, and  $\gamma$  is a scalar coefficient that determines the rate of decrease of kinematic hardening with increasing plastic deformation. According to this evolution law, all stress points should lie within a cylinder of radius  $\sqrt{2/3}\sigma_y$ , where  $\sigma_y$  is the maximum yield stress at saturation. For uniaxial conditions at large plastic strains, when  $\underline{s}$  approaches  $\sigma_y$ ,  $\underline{a}$  becomes equal to  $C/\gamma$ ,  $\dot{\underline{a}}$  tends to zero and

$$\sigma_y = C/\gamma + \sigma_o \quad (3)$$

For clays, the maximum yield stress  $\sigma_y$  is controlled by the undrained shear strength  $S_u$  according to:

$$\sigma_y = \sqrt{3}S_u \quad (4)$$

Consequently, the value of  $\gamma$  can be defined as:

$$\gamma = \frac{C}{\sqrt{3}S_u - \sigma_o} \quad (5)$$

Therefore, for the full description of nonlinear clay response, only three parameters need to be determined: the strength  $S_u$ , the ratio  $E_o/S_u$  (where  $E_o$  is the small-strain soil stiffness), and  $\gamma$ . The model is calibrated against the experimental  $G - \gamma_{xz}$  curves of Vucetic & Dobry [31] for high



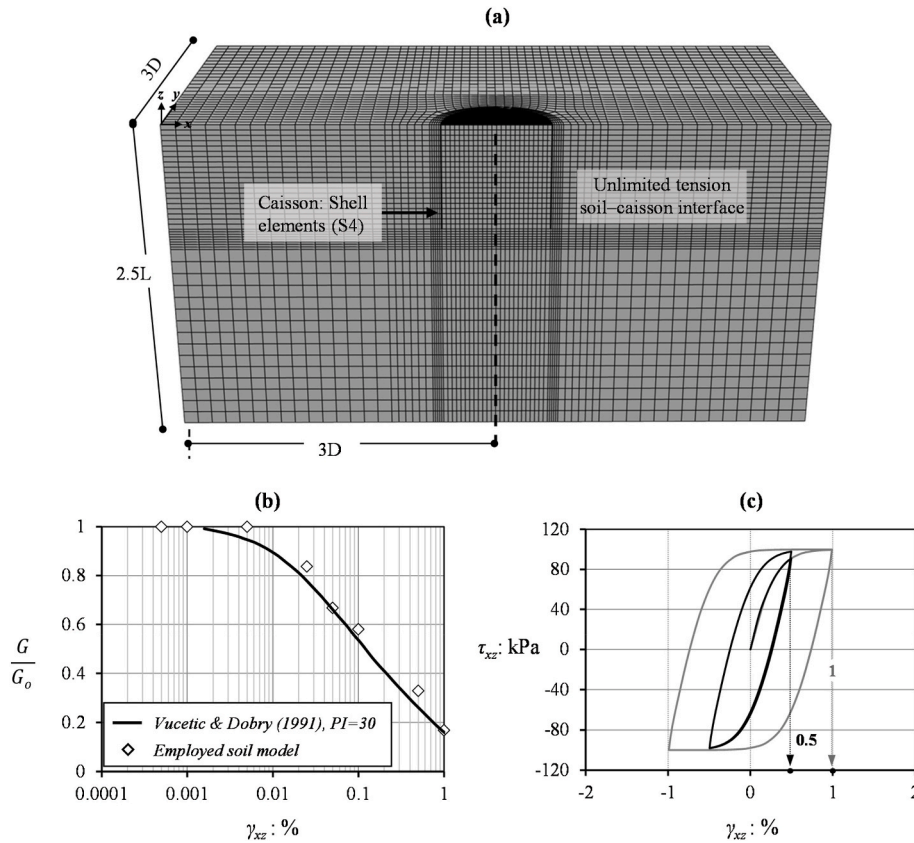


**Fig. 1.** Single suction caisson: (a) FE mesh; (b) Comparison of the  $G-\gamma_{xz}$  curve predicted numerically by the calibrated soil model ( $S_u = 100$  kPa,  $E_o = 180$  MPa) to the experimentally measured curve of [31] for high plasticity clays ( $PI = 30$ ); (c) Hysteresis loops of example clay specimen subjected to cyclic simple shear loading at two characteristic shear strain levels ( $5 \times 10^{-3}$  and  $10^{-2}$ ).

plasticity clays, yielding  $E_o/S_u = 1800$  and  $\gamma = 1154$  (Fig. 1b). Fig. 1c displays typical shear stress – shear strain ( $\tau_{xz} - \gamma_{xz}$ ) loops generated by the calibrated model under quasi-static simple shear loading.

Despite its simplicity, the 3-parameter constitutive model has been extensively validated against physical model tests, demonstrating its effectiveness in describing the overall soil-foundation system response under cyclic loading. Indicative such examples relevant to the present study, involve surface and embedded foundations subjected to cyclic loading and seismic shaking [30] and the cyclic response of piles and caissons subjected to horizontal/moment loading [32].

The suction caisson model is further validated herein against bearing capacity and small-strain stiffness calculations by comparing numerical predictions with available published data. As summarized in Table 1, the computed uniaxial capacity factors compare well to the numerical studies of Hung & Kim [33], Suryasentana et al. [25] and Fu et al. [34],

**Table 1**  
Comparison of numerical predictions with published data for undrained uniaxial capacity factors  $N_{cV}$ ,  $N_{cH}$ ,  $N_{cM}$  and elastic stiffness coefficients  $K_{HH}$ ,  $K_{MM}$ ,  $K_{HM}$  for flexible caissons of  $L/D = 1$  and rough interface conditions.

Uniaxial Capacity Factors			
	$N_{cV}$	$N_{cH}$	$N_{cM}$
<i>This study</i>	12.73	6.15	3.95
[25]   $L/D = 1$	13.00	5.80	3.80
[34]   $L/D = 1$	13.65	-	-
[33]   $L/D = 1$	14.00	6.00	-
Elastic Stiffness Coefficients ( $t_w = 0.024$ m)			
	$K_{HH}$ : MN	$K_{HM}$ : MN	$K_{MM}$ : MNm
<i>This study</i>	2453.3	5585.9	50839.1
[16]	2381.18	5429.1	45347.6

all of which are referring to 3D circular ( $L/D = 1$ ) caisson foundations in homogeneous clay. The vertical capacity factor ( $N_{cV} = V_o/AS_u$ , where  $A = \pi D^2/4$ ) is 9% lower (maximum deviation) compared to the numerical results of [33], while the horizontal capacity factor ( $N_{cH} = H_o/AS_u$ ) displays a 6% difference (maximum deviation) against the solution of [25]. The uniaxial moment capacity factor ( $N_{cM} = M_o/ADS_u$ ) compares well to the study of [25], displaying a mere 4% difference.

Furthermore, the elastic lateral ( $K_{HH}$ ), rocking ( $K_{MM}$ ) and coupled swaying-rocking ( $K_{HM}$ ) stiffness coefficients compare well with the solutions of Gelagoti et al. [16] for relative soil-caisson rigidity ratio equal to  $J = \left(\frac{E_{steel} t_w}{E_o D}\right) = 4.67$ , where  $E_{steel}$  is the Young's modulus of the steel caisson,  $t_w$  is the skirt thickness, and  $D$  is the caisson diameter.

**2.2. Soil-Foundation-Structure (SFS) system**

An 8 MW jacket-supported OWT, installed at a water depth of 60 m in the Adriatic Sea, is used as an illustrative example. The wind turbine and jacket structure characteristics and the environmental load combinations for *Normal* and *Extreme* Sea states were provided by the EU Funded Research Program JABACO [35,36]. The foundation soil corresponds to a clay layer of undrained shear strength  $S_u = 100$  kPa, while the suction caissons are of  $D = L = 6$  m ( $L/D = 1$ ). Table 2 summarizes the turbine tower characteristics, while Fig. 2 illustrates the 3D FE mesh of the

**Table 2**  
Geometric properties of the 8 MW turbine.

	$D_{tower}$ (m)	$t_{tower}$ (m)	$H_{tower}$ (m)	$d_{rotor}$ (m)	Nacelle & Rotor Mass (ton)
8 <sup>MW</sup>	6	0.03	107	164	480

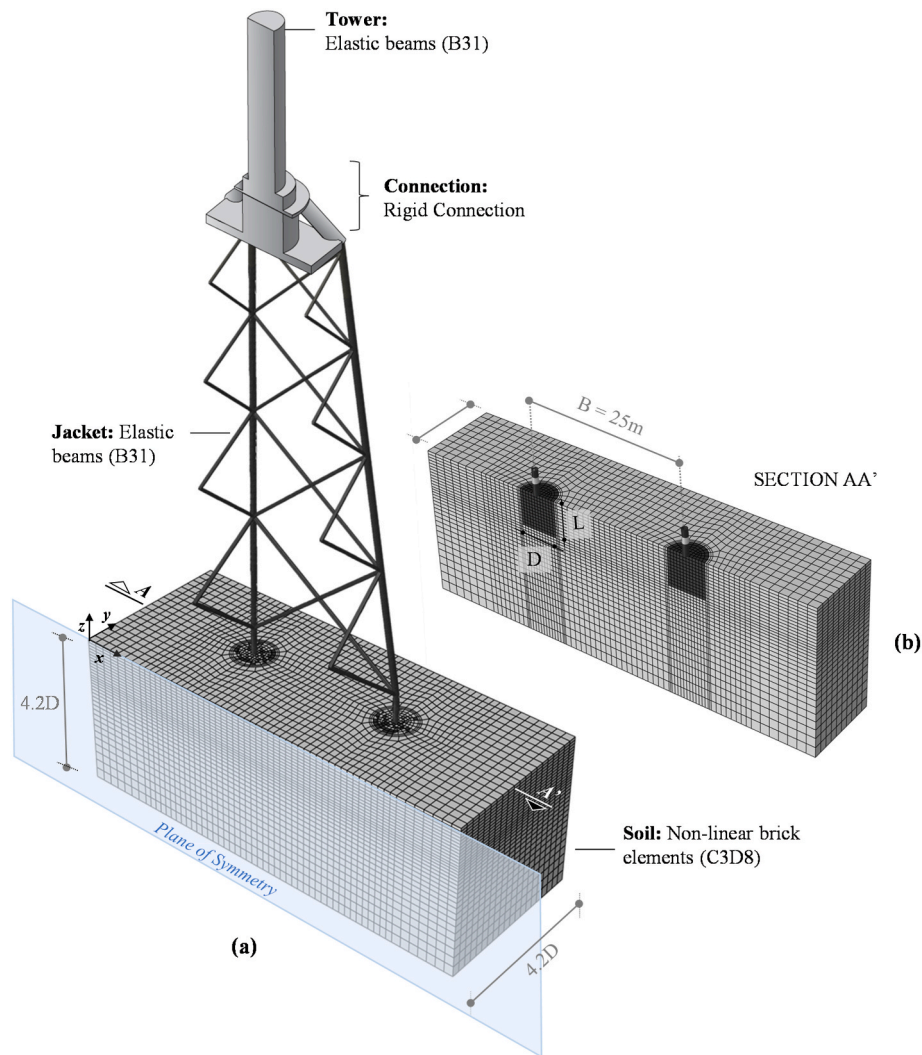


Fig. 2. (a) FE mesh of the global soil–foundation–jacket structure system, and (b) section AA' cut view (caissons & inner soil plug are highlighted with black).

soil–foundation–structure (SFS) system. Details on the geometric properties of the simulated jacket structure are provided in Appendix A. By taking advantage of the problem symmetry, half of the system is modelled. The turbine tower is modelled as an SDOF system, consisting of elastic 3D beam elements (B31) and a concentrated mass at the rotor-nacelle level. The tower is rigidly connected to the top of the jacket, which is also modelled with elastic beam elements (B31). Typical steel material properties are assumed for both the tower and the jacket structure, i.e.,  $E_{steel} = 210$  GPa,  $\nu = 0.2$ , and  $\rho = 7.85$  t/m<sup>3</sup>. Effective density values are considered for the submerged jacket parts.

The suction caissons are modelled as previously described, and are assumed to be fully bonded to the foundation soil (i.e., no separation or detachment is allowed). The assumption is justified by the rapid nature of seismic loading, during which full suction conditions can be assumed beneath the caisson lid (excess pore water pressures cannot dissipate, and passive suction is maintained throughout the shaking).

Compared to the previously discussed static analysis of the single suction caisson, the boundary conditions are modified for the dynamic analyses. Radiation damping is taken into account by introducing dashpots at the base of the model (defined as  $C_{dash} = \rho V_s A$ , where:  $\rho = 2$  t/m<sup>3</sup> is the material density,  $V_s = 350$  m/s the shear wave velocity at the FE model's base, and  $A$  the effective area that corresponds to each dashpot). Appropriate kinematic (MPC) constraints are imposed at the lateral model boundaries to replicate free-field soil response.

### 2.2.1. Benchmark simulation: SBJ OWT subjected to combined seismic and wind loading

For the benchmark simulation, wind loading is approximated by a static wind thrust at the nacelle level – a reasonable assumption, given the low frequency range of wind loading compared to the eigenmodes of the turbine. The analysis is performed in two steps. The structure is initially subjected to a constant horizontal force  $W = 872.2$  kN (corresponding to 70% of the SLS wind load) that generates an overturning moment  $M$  at the jacket base. The jacket provides resistance to this large-amplitude  $M$  through its frame structure; the two windward legs undergo increased vertical load, while the opposite (leeward) legs are unloaded. All jacket legs are also subjected to bi-directional  $H$ - $M$  loading of much smaller amplitude.  $W$  is maintained throughout the second analysis step, during which the model is excited by an acceleration time history (IT.AC.V record from the 2009 L'Aquila earthquake).

Indicative analysis results are summarized in Fig. 3. Acceleration time-histories (Fig. 3a) are plotted for the nacelle level ( $a_{tower}$ ) and at the ground surface ( $a_{surface}$ ). The long-period superstructure (with its first natural period  $T_{1,n} = 4.0$  s away from the dominant earthquake period  $T_E = 0.5$  s) leads to the motion's de-attenuation and a resulting peak acceleration  $a = 0.31g$  at nacelle level. At the time of maximum loading, the Mises stress at the tower and jacket structure is well below the yield point ( $\sigma_{Mises} = 125$  MPa is observed at the right jacket leg at  $t = 3.7s$ , compared to  $f_{yield} = 355$  MPa), confirming the assumption of elastic jacket response.

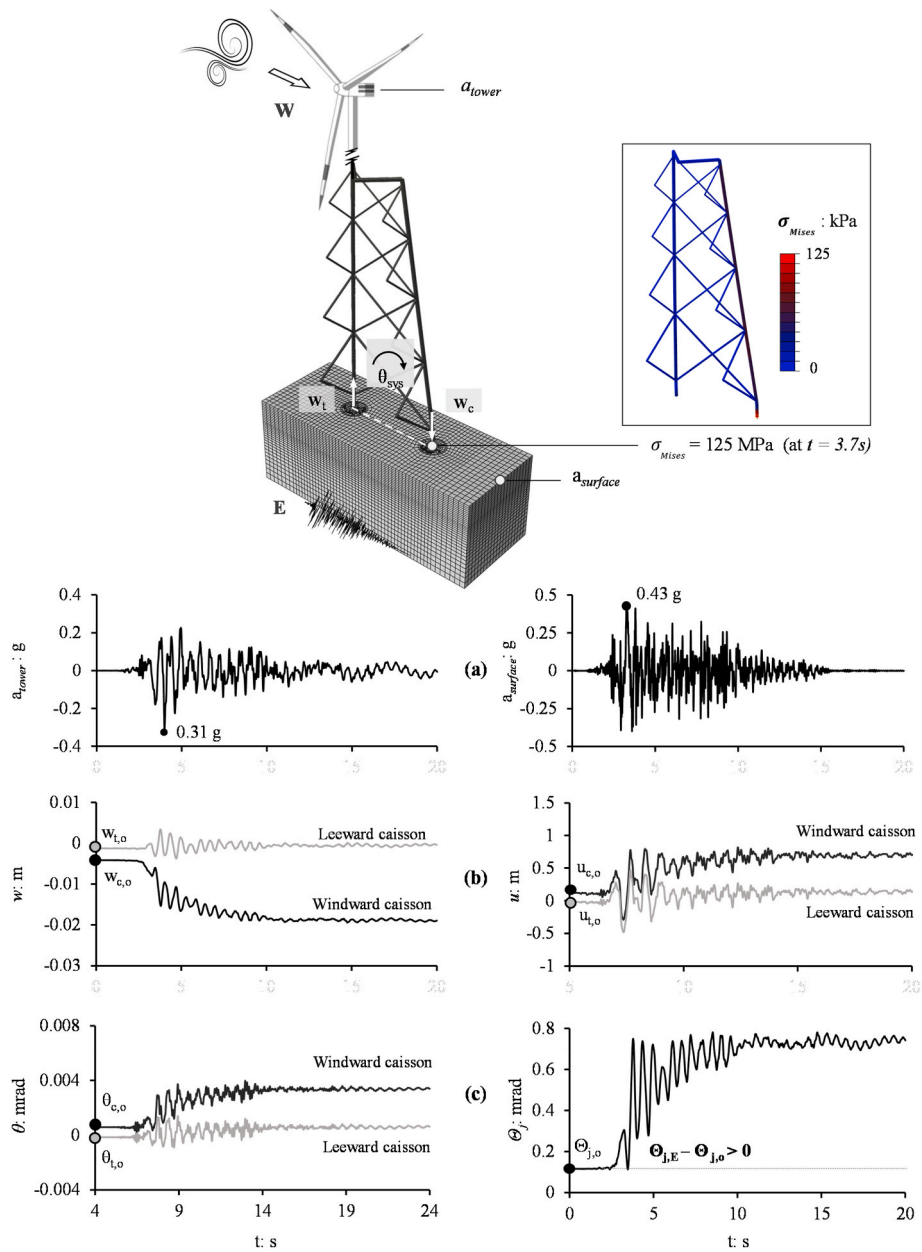


Fig. 3. Performance of the 3D SFS system subjected to combined wind and seismic loading (L' Aquila record). Time histories of: (a) acceleration at tower top ( $a_{tower}$ ) and soil surface ( $a_{surface}$ ); (b) caissons' settlement ( $w$ ) and horizontal displacement ( $u$ ); (c) caissons' rotation ( $\theta$ ) and jacket rotation ( $\theta_j$ ).

Foundation performance is described by the time histories of vertical ( $w$ ) and horizontal ( $u$ ) caisson displacements (Fig. 3b), the rotations at the jacket legs ( $\theta_t$  and  $\theta_c$  for the tensile and compressive leg, respectively), and the rotation ( $\theta_j$ ) of the jacket structure (Fig. 3c). The latter is defined as  $(w_c - w_t)/B$ , where  $w_t$  and  $w_c$  are the vertical displacements of the tensile (leeward) and compressive (windward) leg, respectively, and  $B$  is the width of the jacket. The windward caisson carries a larger initial vertical load compared to the leeward caisson due to the initially applied wind load. This initial load asymmetry leads to an imbalance in the rate of seismic settlement accumulation between the two legs: the compressed (windward) caisson sustains  $w_c = 2$  cm, as opposed to zero settlement of the tensile (leeward) caisson, leading to non-trivial residual jacket rotation  $\theta_j = 0.7$  mrad. Note that, according to DNV-OS-J101 [70], the operational limit for the specific configuration is  $\theta_{lim,SL5} = 4.4$  mrad. The windward caisson also accumulates larger horizontal displacement  $u_c$  and rotation  $\theta_c$  (Fig. 3b), which are, however, not large

enough to constitute a threat.

### 3. "Caisson-on-Winkler-Soil" (CWS) model

Winkler-based models simplify the problem by replacing the soil with a series of uniformly distributed independent springs and dashpots. Such models have been widely used for the design and performance assessment of laterally and axially loaded piles (e.g. [37–43]). Gerolymos & Gazetas [44–46] and Assimaki et al. [47] proposed an extension for cylindrical embedded foundations. A 4-spring model was introduced (including four sets of springs and dashpots) to account for the coupled swaying-rocking response of rigid caisson foundations in multi-layered soils. A similar model was employed by Tsigginos et al. [48] to study the seismic response of a caisson-bridge pier system.

A fundamental limitation of existing models is their inability to account for deformation accumulation. Even when nonlinear spring re-

lations are employed (e.g., the  $p - y$ ,  $t - z$  methods proposed by API [42]), these are still elastic and, therefore, limited to monotonic loading. Modelling permanent deformation accumulation requires introducing nonlinear hysteretic elements, which is the scope of this study.

### 3.1. General description

The proposed "Caisson-on-Winkler-soil" (CWS) model is essentially a nonlinear hysteretic variation of the 4-spring Winkler model, extended to incorporate the coupling of vertical – horizontal – moment (VHM) loading, as well as permanent deformations under dynamic loading. As shown in the schematic of Fig. 4a, a rigid body motion is assumed for the suction caisson and the inner soil plug. This is a reasonable simplification for seismic loading, during which the soil-caisson interface is expected to maintain full contact, thanks to the development of negative pore pressures below the lid. Based on this assumption, the caisson and the inner soil plug are modelled as a rigid body of equivalent density, the response of which under combined  $V - H_x - M_y$  loading is schematically shown in Fig. 4b. The caisson head is used as a reference, with the vertical and horizontal displacement and rotation denoted by  $v$ ,  $u$ , and  $\theta$ , respectively.

The CWS model comprises an assembly of distributed and concentrated hysteretic elements: (i) vertical distributed elements ( $k_z$ ) along the caisson shaft; (ii) horizontal distributed elements that represent the normal ( $k_{x,n}$ ) and frictional ( $k_{x,s}$ ) resistance of the sides to lateral loading; (iii) a concentrated vertical element at the caisson base ( $K_{bz}$ ), linked to the base axial resistance; (iv) a concentrated horizontal element ( $K_{bx}$ ) at the base, which represents the base contribution to the lateral resistance mechanism; and (v) a concentrated rotational element at the base ( $K_{b\theta}$ ), which provides the base resisting moment due to normal stresses. The distributed vertical elements on the sides serve a dual purpose, simultaneously contributing to both the axial shaft resistance and the rotational resisting mechanism. The latter is captured by the overturning moment  $M_y = \sum m_y = \sum k_z w D$  (Fig. 4b), generated by the differential vertical movement  $w$  between the caisson sides. Such modelling allows the physical coupling between the axial and rotational response of the shaft.

Since spring elements cannot incorporate hysteresis, nonlinear 1D hysteretic truss elements (T3D2) are employed instead. A considerable length (e.g.,  $L = 10$  m) is necessary to minimize the error related to second-order effects during large deformations. Their nonlinear response follows a kinematic hardening constitutive model with Von

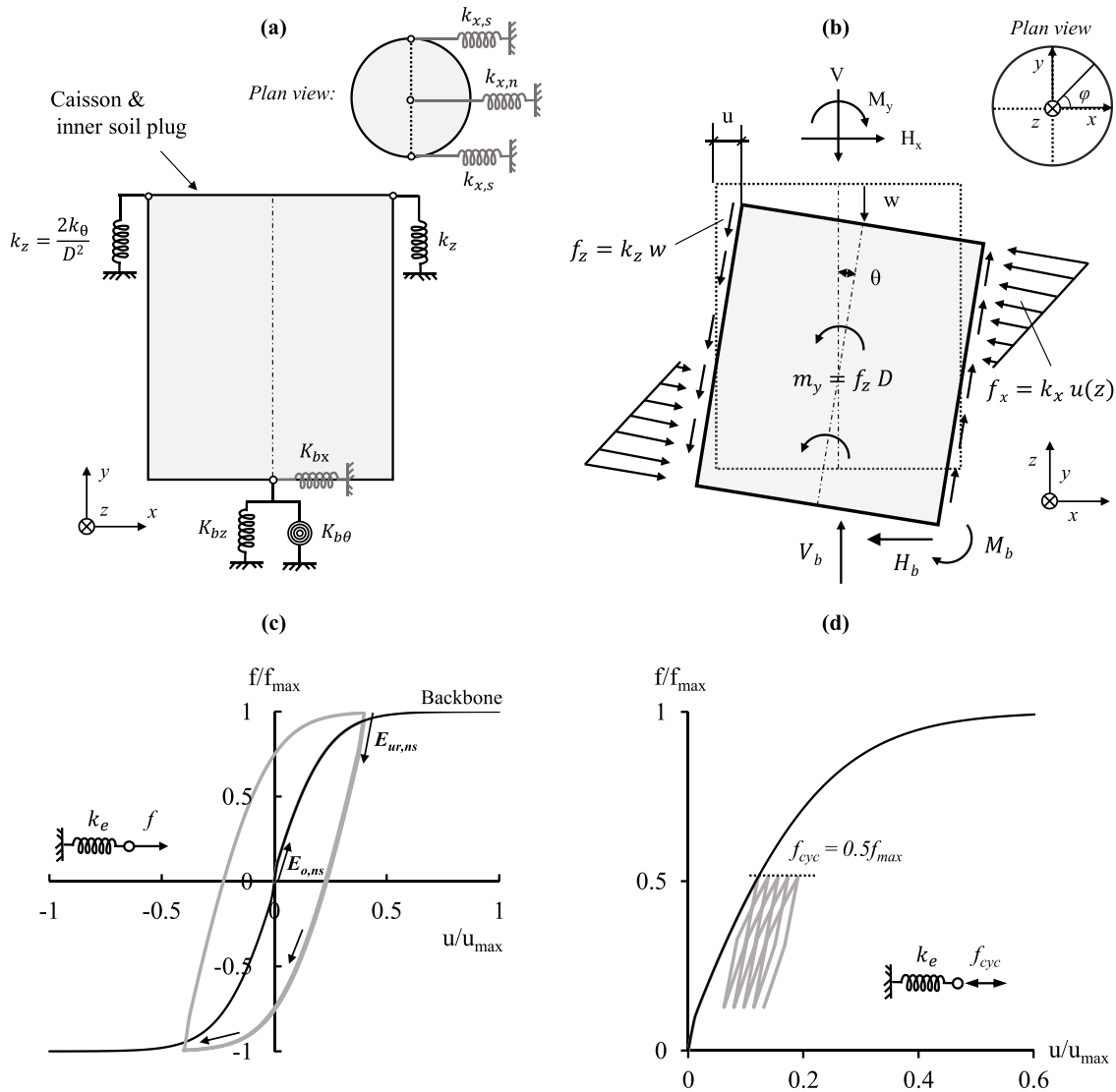


**Fig. 4.** 'Caisson-on-Winkler-Soil' model: (a) schematic illustration of the model; (b) rigid body response of the caisson subjected to VHM loading at the top. Nonlinear hysteretic element response: (c) backbone curve and two-way cyclic loading at  $0.4u_{max}$ ; and (d) one-way cyclic loading at half of the maximum yield stress.



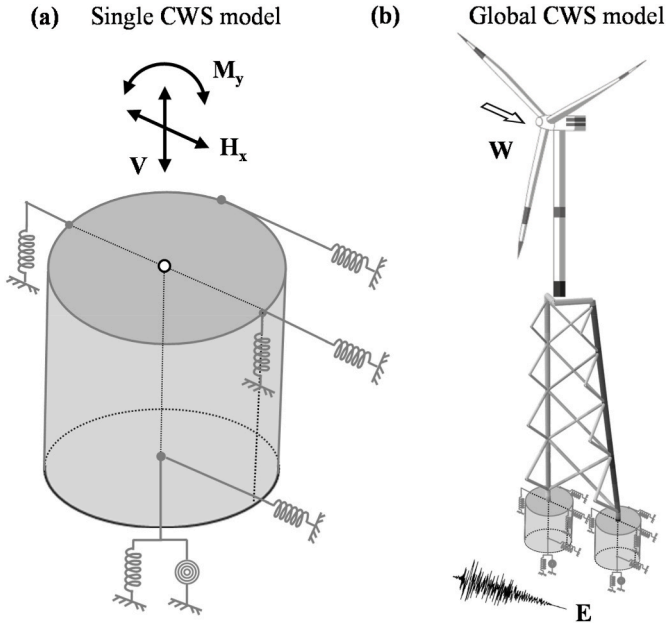


Fig. 5. Simplified model configurations used in the comparison of the CWS model to the rigorous 3D FE model: (a) the single CWS model, and (b) the global CWS model.

Mises failure criterion and associated flow rule (similar to the one previously described for the detailed 3D model). For the hysteretic truss elements, the model is defined by a small-strain stiffness modulus ( $E_{o,ns}$ ), a yield point ( $\sigma_y$ ), and hardening parameters that describe the post-yield response. As shown in Fig. 4c, their uniaxial behaviour follows a backbone curve, while the unloading/reloading response satisfies the Masing rule, which implies that the unloading–reloading modulus ( $E_{ur,ns}$ ) is equal to the small-strain modulus. ( $E_{o,ns}$ ).

The small-strain stiffness modulus ( $E_{o,ns}$ ) is calculated based on the uniaxial elastic stiffness ( $k_e$ ) of each hysteretic element:

$$E_{o,ns} = k_e L / A \quad (6)$$

where:  $L, A$  are the element length and area, respectively. The maximum yield stress is equal to the ultimate soil reaction force of the element ( $\sigma_y = f_{max}$ ). Fig. 4(c,d) displays indicative examples of force–displacement time-histories of a caisson experiencing two-way symmetric and one-way asymmetric cyclic loading. Under asymmetric loading ( $f_{cyc} = 0.5f_{max}$ ), the element captures the accumulation of plastic strains with subsequent loading cycles without exhibiting signs of ratcheting (Fig. 4d).

### 3.2. CWS model calibration

#### 3.2.1. Small strain stiffness

The calibration of the small-strain stiffness of the hysteretic elements is based on 3D FE calculations, following the flexibility approach of Assimaki et al. [47]. A unit lateral force and a unit overturning moment are applied at the top of the 3D caisson model, allowing the computation of the lateral ( $K_{HH}$ ), rocking ( $K_{MM}$ ), and cross-lateral rocking ( $K_{HM}$ ) stiffnesses. 3D FE modelling for calibration purposes may be avoided, using the previously discussed readily available closed-form solutions. Via horizontal force and moment equilibrium at the top of the caisson, the values of distributed ( $k_x, k_z$ ) and concentrated base ( $K_{bx}, K_{b\theta}$ ) horizontal and rotational stiffnesses are deduced as follows:

$$k_x = 2 \left( \frac{K_{HH}L + K_{HM}}{L^2} \right) \quad (7)$$

$$K_{bx} = - \frac{K_{HH}L + 2K_{HM}}{L} \quad (8)$$

$$K_{MM} = (k_z D^2 / 2)L + K_{b\theta} + \left( k_x \frac{L^3}{3} + K_{bx} L^2 \right) \quad (9)$$

In order to calculate the distributed  $k_z$  based on Eq. (9),  $K_{b\theta}$  may be defined by evaluating the rotational stiffness of a diameter  $D$  surface foundation, founded on a 6 m deep open trench (for the case examined), applying unitary overturning moment at the top (seabed). The closed-form solution of Gazetas [49] can be used:

$$K_{b\theta} = \frac{1}{3} \frac{GD^3}{(1-\nu)} \quad (10)$$

where:  $G$  and  $\nu$  are the soil shear modulus and Poisson's ratio. The same rationale applies to the vertical base coefficient  $K_{bz}$ , which may be calculated as [50]:

$$K_{bz} = \frac{2.01 GD}{(1-\nu)} \left( 1 + 0.195 \frac{L}{D} \right) \quad (11)$$

Nevertheless,  $K_{bz}$  and  $K_{b\theta}$  are computed herein based on the 3D FE model to allow their direct comparison. For the studied problem, the computed  $k_x, k_z, K_{bx}, K_{b\theta}$  and  $K_{bz}$  are summarized in Table 3.

The *dynamic* stiffnesses of the 1D hysteretic elements are calculated as products of the above *static* stiffnesses and a dynamic stiffness coefficient  $\Delta(\omega)$ . The latter is a function of the dimensionless frequency  $\alpha_0 = \omega D / V_s$ , where  $\omega$  is the angular frequency of the excitation, and  $V_s$  the shear wave velocity of the soil profile. They are derived according to the formulas proposed by Assimaki et al. [47], based on the value of  $\alpha_0$  of each studied scenario. For the cases examined herein, the dynamic coefficient  $\Delta(\omega)$  ranges between 0.9 and 1.0, and, therefore, the *dynamic* stiffnesses are very close to the *static* stiffnesses of Table 3.

#### 3.2.2. Ultimate strength ( $f_{max}$ )

The ultimate strength of the hysteretic elements is calibrated through the following three steps: (1) estimation of global (uniaxial) caisson capacities ( $V_o, H_o, M_o$ ); (2) estimation of local capacity factors (i.e., the contribution of the shaft and base resistance); and (3) distribution of local capacities to individual hysteretic elements (i.e., assignment of  $f_{max}$ ). The purely vertical resistance  $V_o$  can be calculated on the basis of 3D FE push-down analyses (assuming that the capacity is reached at  $w = 0.01 D$ ), which also allow to distinguish between base ( $V_b$ ) and shaft ( $V_{shaft}$ ) resistance. Readily available global and local capacity factors ( $N_{cV}$ ) from the literature (e.g. [34]) can also be used, or experimental results (if available). The analysis conducted herein is based on the 3D FE analysis employing the kinematic hardening model, but more sophisticated constitutive models can also employ the same calibration procedure.

As summarized in Table 4, the computed base resistance  $V_b$  is assigned to the vertical hysteretic element at the base of the caisson, while the ultimate shaft capacity  $V_{shaft} = N_{cV, shaft} AS_u = 11.3$  MN is equally distributed to the vertical peripheral elements of the shaft, such that:

Table 3

Computed stiffnesses of the CWS model for the studied problem.

Hysteretic element	Type	Static Stiffness
Horizontal /Shaft	Distributed	$k_x = 507.4$ MN/m <sup>2</sup>
Vertical /Shaft	Distributed	$k_z = 227.2$ MN/m <sup>2</sup>
Horizontal /Base	Concentrated	$K_{bx} = 591.3$ MN
Rotational /Base	Concentrated	$K_{b\theta} = 11051.2$ MNm
Vertical /Base	Concentrated	$K_{bz} = 1367.3$ MN

**Table 4**  
Best-fit local capacity factors assigned to the CWS model elements.

Global	Local Uniaxial Capacity Factors		
$N_{cV}$	$N_{cV, base} (V_b)$	$N_{cV, shaft} (V_{shaft})$	
10.32 <sup>a</sup>	6.32	4.00	
$N_{cH}$	$N_{cH, shaft, s} (H_{shaft,s})$	$N_{cH, shaft, n} (H_{shaft,n})$	$N_{cH, base} (H_b)$
6.15	1.41	4.37	0.37
$N_{cM}$	$N_{cM, base} (M_b)$	$N_{cM, shaft, x} (M_x)$	
3.95	0.72	2.00	

<sup>a</sup> at  $w = 0.01D$ .

$$V_{shaft} = \int_0^L \int_0^{2\pi} \left( f_{max,kz} \frac{D}{2} \right) d\varphi dz = N_{cV, shaft} A S_u \quad (12)$$

where:  $f_{max,kz}$  is the unit soil reaction of the vertical distributed elements expressed in  $kN/m^2$ , and the angle  $\varphi$  is defined in Fig. 4b. It should be noted that the vertical truss elements are assigned equal resistance for pull-out and push-down loading, justified by the assumption of full suction beneath the caisson lid. Under pure moment loading ( $M_o$ ), the failure mechanism is a combination of scoop and wedge-sliding mechanisms, primarily driven by shear and normal stresses at the caisson shaft and the normal stresses developed at the caisson base. The contribution of the base to moment resistance ( $M_b$ ) is calculated according to Suryasentana et al. [25], yielding a local moment capacity factor equal to  $N_{cM, base} = 0.72$ . The shaft resisting moment ( $M_{shaft}$ ) involves the aggregation of two stress distributions: (i) the moment generated by the vertical shear stresses developed on the shaft ( $M_{shaft,y}$ ); and (ii) the moment generated by the horizontal stresses ( $M_{shaft,x}$ ), which also contribute to the horizontal soil reaction. With  $M_{shaft,y} = (\sum f_z) D$  (where  $\sum f_z = V_{shaft}/2$ ), the capacity of the vertical distributed hysteretic elements ( $f_{max,kz}$ ) is computed so that:

$$M_{shaft,y} = \int_0^L \int_0^{2\pi} \left( f_{max,kz} \frac{D^2}{4} \right) d\varphi dz = N_{cM, shaft,y} ADS_u \quad (13)$$

The remaining shaft moment capacity ( $M_{shaft,x} = M_{shaft} - M_{shaft,y}$ ) is provided by the horizontal distributed hysteretic elements ( $f_{max,kx,n}$  and  $f_{max,kx,s}$ ).

Under pure lateral loading ( $H_o$ ), the failure mechanism is the combination of a (broader) wedge-sliding mechanism above the skirt-tip level and a scoop mechanism beneath the skirt-tip level. Following the study of [25], similar values of lateral resistance per meter of length are assigned to the base ( $H_b$ ) and shaft ( $H_{shaft}$ ) elements. The horizontal shaft reaction is the resultant of two stress distributions: the passive and active pressures developed on the two sides perpendicular to the loading direction ( $H_{shaft,n}$ ), and the horizontal shear tractions on the sides parallel to the loading direction ( $H_{shaft,s}$ ). Activation of 70% of the lateral frictional resistance ( $H_{shaft,s} = S_u \times \pi DL/2$ ) is assumed in the case of pure horizontal loading, based on the results of the 3D FE analyses. The remaining lateral capacity is assigned to the distributed horizontal hysteretic elements of the shaft and the concentrated base element in a uniform manner, so that:

$$H_{shaft, n} = \int_0^L \int_0^{\pi} \left( f_{max,kx,n} \frac{D}{2} \right) d\varphi dz = N_{cH, shaft, n} AS_u \quad (14)$$

$$H_{shaft, s} = \int_0^L \int_0^{\pi} \left( 0.70 f_{max,kx, s} \frac{D}{2} \right) d\varphi dz = N_{cH, shaft, s} AS_u \quad (15)$$

where:  $f_{max,kx,n}$  and  $f_{max,kx,s}$  are the sought values of ultimate soil reactions of the horizontal distributed hysteretic elements (normal and frictional, respectively), expressed in  $kN/m^2$ .

The computed local capacity factors for all model elements are

summarized in Table 4 for the problem studied herein. It should be noted that for  $L/D > 1$ , the failure mechanisms for  $H_o$  or  $M_o$  are expected to change [34], and therefore the local capacity factors presented herein will no longer be valid. Moreover, the pure horizontal and moment capacities are affected by the presence of vertical load  $V$ : the larger the vertical capacity ratio ( $V/V_o$ ), the lower the resulting  $H_o$  and  $M_o$  capacities. However, the values of  $H_o$ ,  $M_o$  corresponding to  $V = 0$  remain approximately valid for  $V/V_o \leq 40\%$ , as indicated by Yun & Bransby [51], and Gouvernec & Barnett [19]. In the current study of combined wind and earthquake ( $W + E$ ) loading, the static wind action leads to  $V/V_o = 0.25$  for the critical windward caisson, and therefore the effect of  $V$  can be ignored in  $H - M$  calculations. In the case of  $V/V_o > 40\%$ , the readers are referred to [19] to quantify the effect of  $V$  on  $H_o$ ,  $M_o$ .

#### 4. CWS vs. detailed 3D FE models: comparison of performance

This section aims to assess the performance of the proposed CWS model, using the rigorous 3D FE model as a benchmark. The models are initially compared in terms of uniaxial and coupled monotonic horizontal–moment response, being subsequently tested in terms of seismic deformation predictions. The section offers below an overview of the ensemble of FE models employed in the analyses to assist the readers’ understanding. More specifically, four models are utilized (two spring models and two rigorous 3D FE models), hereafter termed as:

- Single CWS model (Fig. 5a)
- Global CWS model (Fig. 5b)
- Single 3D FE model (Fig. 1a)
- Global 3D FE model (Fig. 2a).

##### 4.1. Uniaxial capacities & H–M failure envelope

Fig. 6 compares the single CWS model to the single 3D FE model (used as a benchmark) under (a) vertical, (b) horizontal, and (c) moment loading, confirming the efficiency of the calibration procedure in terms of uniaxial capacities. Fig. 7 extends the comparison in the  $H - M$  space. The displacement-controlled probe tests conducted with the 3D model match very well the normalised  $H - M$  failure envelope ( $V/V_o = 0$ ) of [25]; further confirming its validity (Fig. 7a). The CWS model predictions are excellent in the first quadrant of the  $H - M$  space, where the applied  $H$ ,  $M$  loads share the same sign. However, the model fails to reproduce the failure envelope on the second quadrant, exhibiting a clear cut-off of the horizontal caisson capacity at  $H_o$ . This is hardly a surprise, as the model was calibrated based on  $H_o$ ,  $M_o$  capacities, aiming to realistically capture the response on the 1<sup>st</sup> quadrant, where the examined ( $W + E$ ) loading scenarios occur. Finally, Fig. 7(c,d) presents the good comparison of the single CWS model to the single 3D FE model for three  $H - M$  load paths, corresponding to  $M/H$  ratios expected for the windward suction caisson of the examined jacket OWT, due to environmental loading.

##### 4.2. Seismic deformation predictions

The proposed CWS model is tested herein per its ability to reproduce the foundation deformations of a jacket OWT under transient irregular VHM loading. The latter is generated by the combined action of a steady wind force at the nacelle level (70% of the SLS wind thrust at Normal Sea state) and seismic excitation. The IT.AC.V record (2009 L’Aquila earthquake) and the Tabas-LN record (1978 Tabas earthquake) are used as seismic excitation, referred to hereafter as Scenarios 1 and 2, respectively (Fig. 8). Two comparisons are performed, and the results are presented in Fig. 9 and Fig. 10:

- Two caissons, represented by the single CWS model and the single 3D FE model, are subjected to identical  $V - H_x - M_y$  time



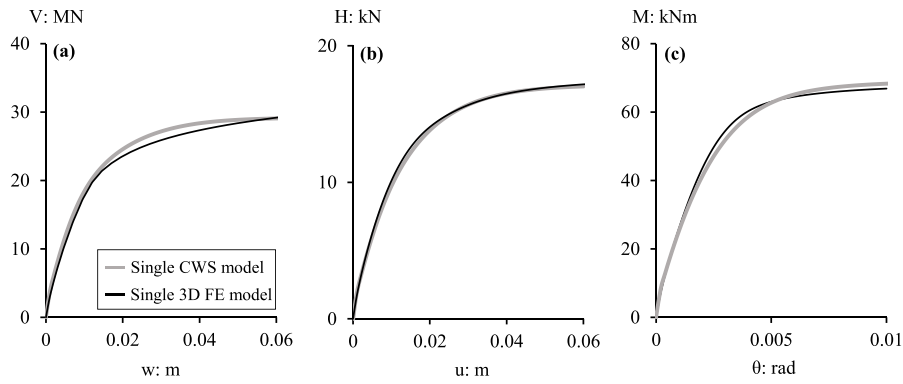


Fig. 6. Comparison of the single CWS model against the single 3D FE model against: (a) vertical; (b) horizontal; and (c) moment loading.

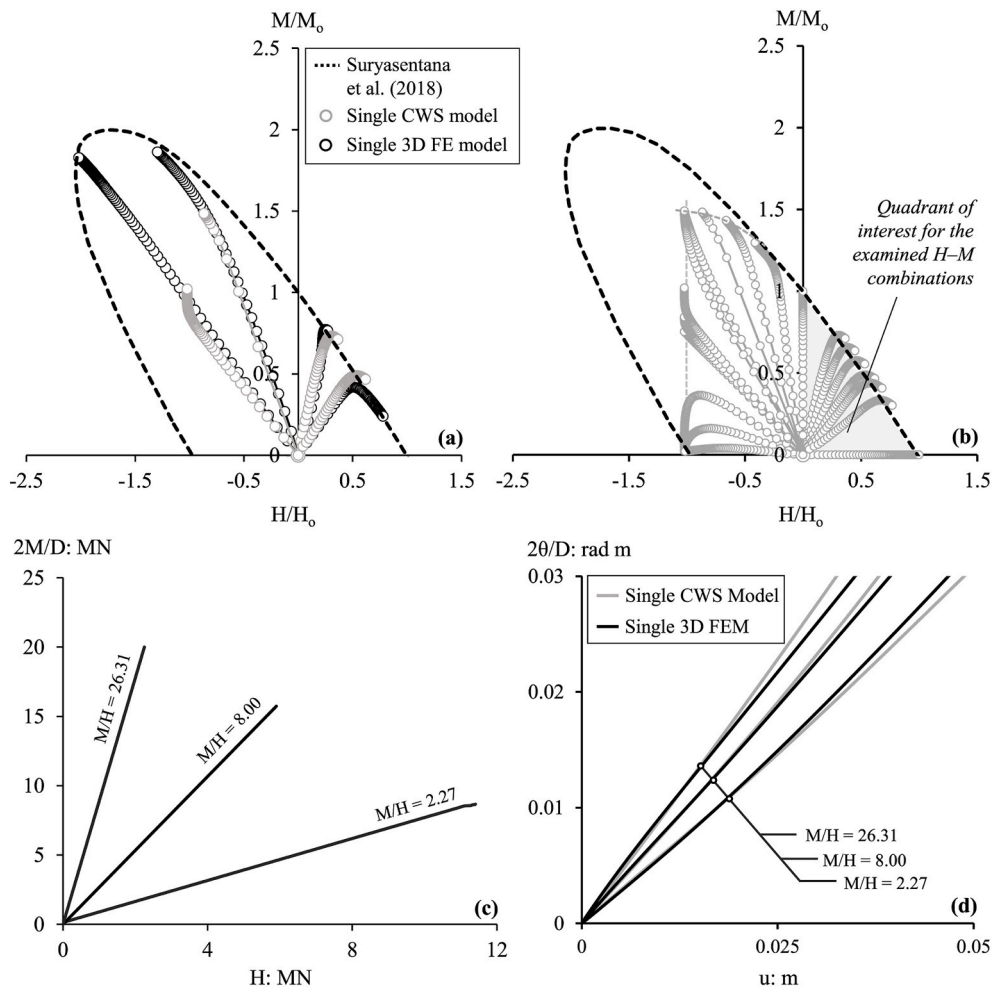


Fig. 7. Comparison of the single CWS model against the single 3D FE model in the  $H-M$  space: (a) displacement-controlled probe tests ( $V/V_0 = 0$ ), compared to the  $H-M$  failure envelope of [25]; (b) CWS model failure envelope ( $V/V_0 = 0$ ), (c) examined  $M-H$  load-controlled paths; and (d) single CWS vs. 3D FE model response for the examined load-controlled probe tests.

histories at their heads. The applied loads correspond to the inertial forces acting at the windward leg of the jacket, calculated through structural analysis of the above-ground system under wind and earthquake loading.

(b) The global CWS and 3D FE systems of the SBJ wind turbine are subjected to combined wind and earthquake loading.

The following observations are worthy of note:

- When the single caisson is subjected to external loading (attributed to the inertial loading of the jacket), the performance of the CWS model (against the rigorous single 3D FE model) is excellent, both in terms of accumulation rate and permanent deformation (Fig. 9). The CWS model successfully reproduces all the key nonlinear and dynamic characteristics of the simulated caisson in both scenarios, while effectively reducing the average computational time by almost two orders of magnitude (80 times). The strong coupling between

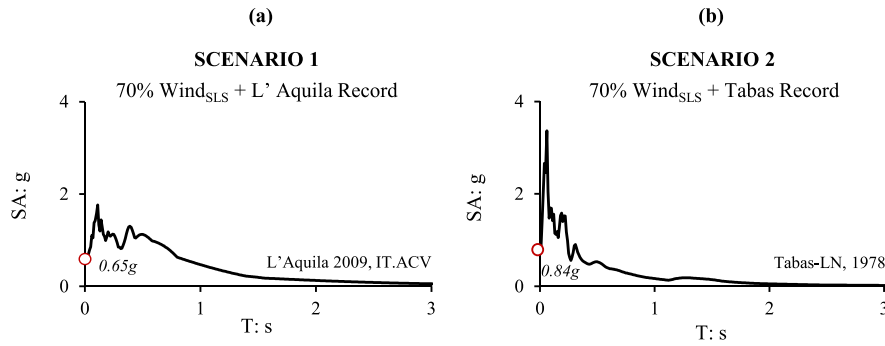


Fig. 8. Seismic excitation scenarios for the comparison of the CWS models to the detailed 3D FE models in terms of seismic deformation predictions.

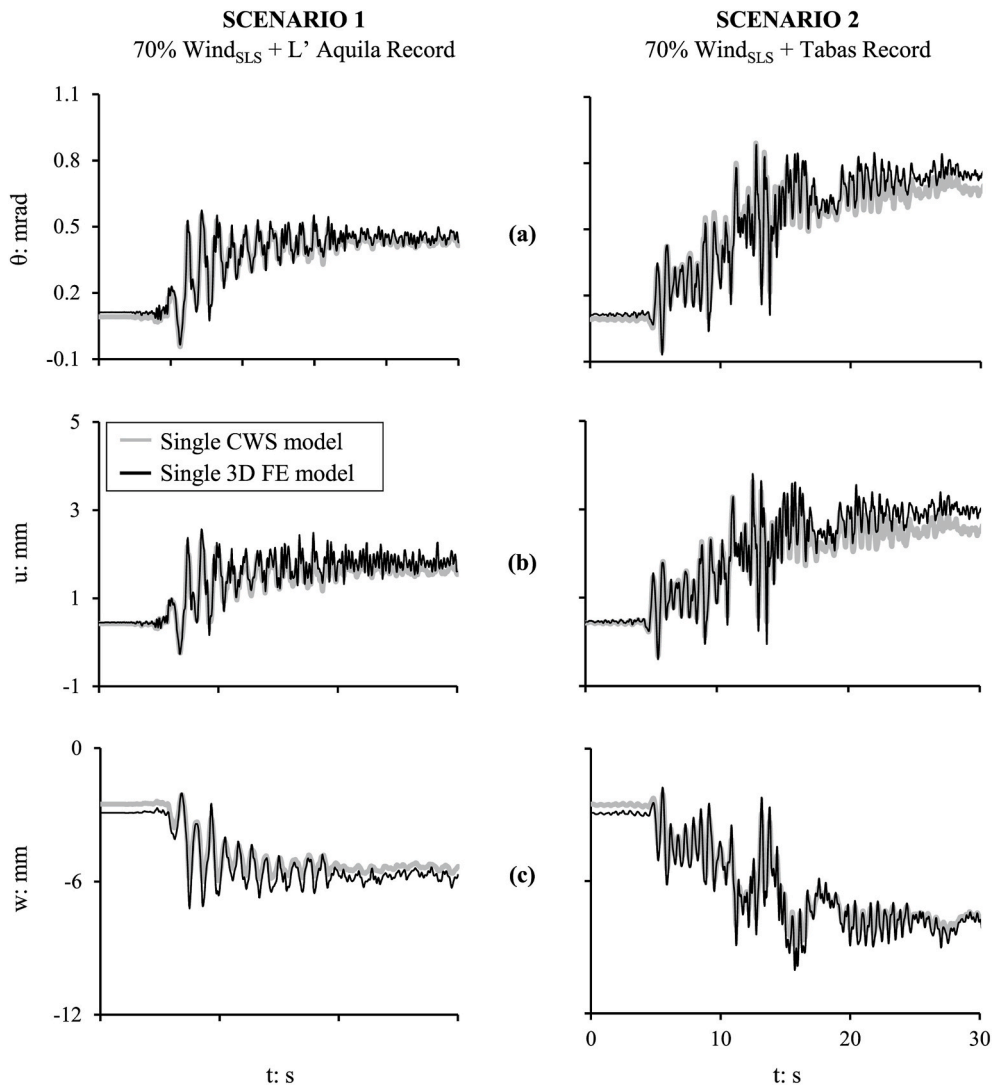


Fig. 9. Comparison of the single CWS and 3D FE models for Scenarios 1 and 2. Time histories of: (a) caisson rotation  $\theta$ ; (b) caisson horizontal displacement  $u$ ; and (c) caisson settlement  $w$ .

settlement and accumulation of rotation is worth noting: large vertical loads ( $V$ ) push the sidewall  $k_z$  elements into their post-yield regime, leading to plastic deformations along the shaft. These are ultimately responsible for a non-trivial accumulation of caisson rotation ( $\theta$ ) during strong earthquake shaking. Under inertial  $VHM$  loading, the single 3D FE model produces significantly lower caisson

deformations, compared to the global 3D FE model under combined wind and earthquake loading (benchmark simulation). The reasons behind such discrepancy are revisited later on in Section 5

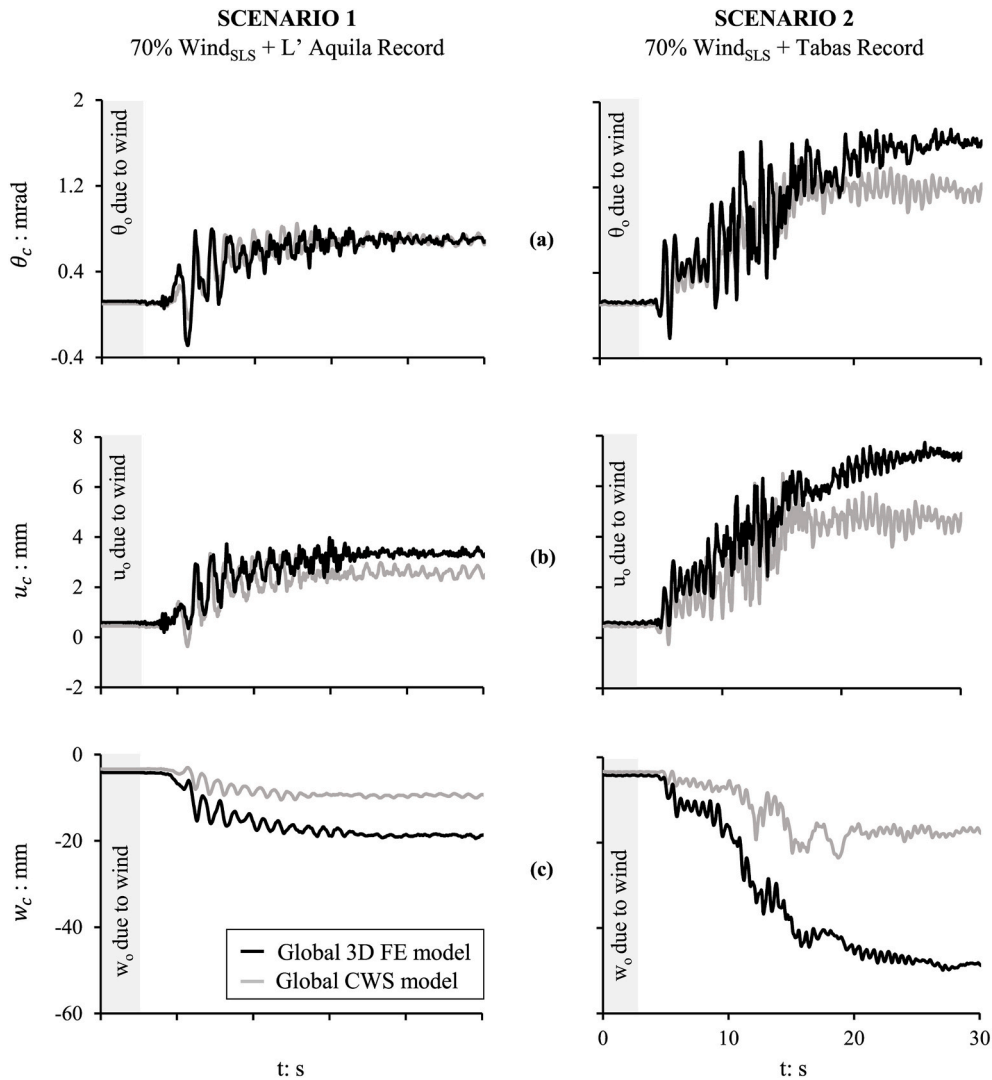


Fig. 10. Comparison of the global CWS and 3D FE models for Scenarios 1 and 2. Time histories of: (a) windward caisson rotation  $\theta_c$ ; (b) windward caisson horizontal displacement  $u_c$ ; and (c) windward caisson settlement  $w_c$ .

- The global CWS model underpredicts the seismically accumulated settlements of the windward leg for both earthquake scenarios. For example, the CWS model predicts a 20 mm residual settlement at the windward leg after the Tabas (1978) earthquake when the actual value (derived by the global 3D FE model) is 50 mm. The reason behind this poor performance is the distinctive stressing combination generated by the concurrent action of wind & earthquake loading (which was not present in the previous comparison, where the loading was externally applied). Here, the foundation of the jacket is subjected to combined loading, stemming on the one hand from soil shearing due to the propagating earthquake waves (*kinematic* loading), and shearing due to the *inertial* loading of the superstructure. Not surprisingly, such a dual-shearing mechanism cannot be captured by the global CWS model, where the stressing of the horizontal  $k_x$  elements (due to the seismic excitation) is entirely uncorrelated to the stressing of vertical  $k_z$  elements. The subsequent section will provide a detailed presentation of this distinctive accumulation mechanism.

On the other hand, the rotation and displacement predictions of the global CWS model are satisfactory. The CWS simulation competently captures the settlement-rotation coupling (as already discussed) while being sensitive to the seismic wave propagation effects responsible for

non-uniform acceleration distribution along the caisson skirt, which also affects the ultimately developing deformations. In the specific example, due to this very effect, the rotation  $\theta_c$  of the windward caisson is increased to 1.2 mrad, while the horizontal displacement  $u_c$  to 4 mm during the Tabas 1978 event (compared to the 0.65 mrad and 2.4 mm of Fig. 9, respectively).

In a nutshell, the proposed CWS model is shown to be appropriate for analysing the foundation response of SBJ OWTs under any combination of externally applied environmental loading (wind/waves time-histories applicable to power production or idling load cases of OWTs). When it comes to the seismic performance of SBJ OWTs, the CWS may be used for estimating rotations and displacements at the caisson level. However, it is not recommended for assessing the co-seismic settlements of the caissons (and hence the global rotation of the jacket frame).

In this regard, the following section explores in greater detail the mechanism of co-seismic settlement accumulation and proposes an engineering-based methodology for diagnosing the severity of its impact on the OWT performance.

### 5. Co-seismic caisson settlements

#### 5.1. Generation mechanism

As witnessed by the previous discussion, seismically excited caissons may experience increased settlements that exceed those experienced in non-seismic load cases. To illuminate the factors contributing to this striking deformation pattern, we analyze herein the single 3D FE model under two alternative loading scenarios (Fig. 11):

- (a) Caisson bearing an initial static load of  $V_w = 9.2$  MN is subjected to seismic shaking (applied at the model base), idealized by a Tsang-type pulse having a predominant frequency of  $f_E = 1.5$  Hz and peak acceleration  $a = 0.4g$ .
- (b) Caisson bearing the same initial static load  $V_w$  is subjected to dynamic cyclic loading  $V_{dyn}(t)$  of frequency  $f_E = 1.5$  Hz, applied at the caisson head. The amplitude of  $V_{dyn}$  is appropriately chosen to result in the same level of shear stress & strain as the seismic excitation (at the soil elements of the caisson shaft).

The results are shown for two characteristic elements, in the middle of the caisson shaft, one on the left (1) and a second (2) on the right (Fig. 11a; 11b). As evidenced by the stress-strain loops of Fig. 11c, the

two loading scenarios are equivalent in shear stresses and shear strains at these representative locations.

Fig. 12 compares the two loading scenarios in terms of shear strain ( $\gamma_{xz}$ ) time histories at the two characteristic soil elements (Fig. 12a), shear strain contours (Fig. 12b), and caisson settlement time histories (Fig. 12c). To focus on the dynamic (cyclic or shaking) part of the response, the shear strains imposed by the initial vertical load  $V_w$  have been subtracted from the respective time – histories and contour plots of Fig. 12. Although the caisson is subjected to the same level of  $\gamma_{xz}$  there is a distinctive difference between the two loading scenarios (Fig. 12a). The time history of  $\gamma_{xz}$  of the two soil elements is identical in the case of cyclic loading, which is not the case for the seismic scenario where the two elements demonstrate a phase shift in their response. This difference is further elucidated when comparing the shear strain contours of Fig. 12b. Once again, during cyclic loading, the two elements can be seen to sustain symmetric straining for the cyclic loading scenario: at times  $t_1$  and  $t_2$  (corresponding to a positive and a negative peak of  $V_{dyn}$ ), the two elements experience the same shear strain ( $\gamma_{V,1} = \gamma_{V,2}$ ). The vertical displacement of the caisson is directly correlated to the direction of the imposed cyclic load  $V_{dyn}$ . When  $V_{dyn} < 0$  (pull out) the caisson settles, moving back upwards when  $V_{dyn} > 0$  (compression). As shown in Fig. 12c, this leads to accumulation of settlement only when the caisson is subjected to compressive  $V_{dyn}$ .

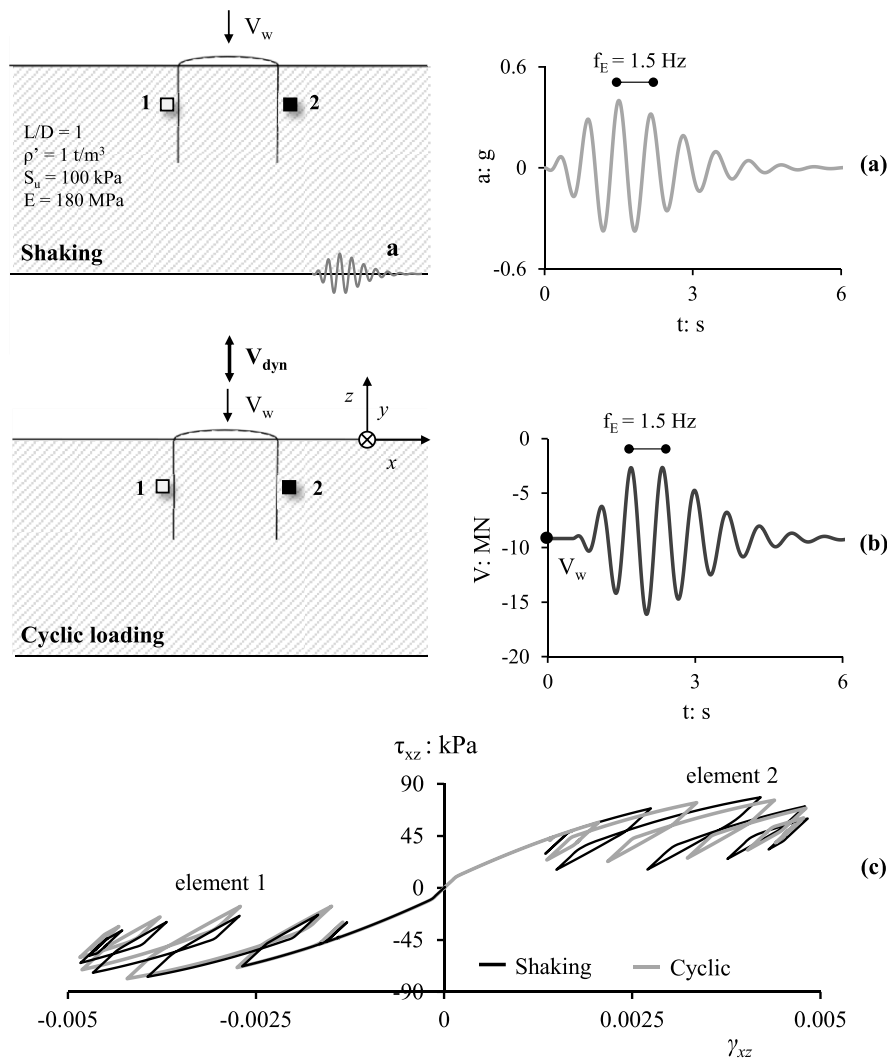
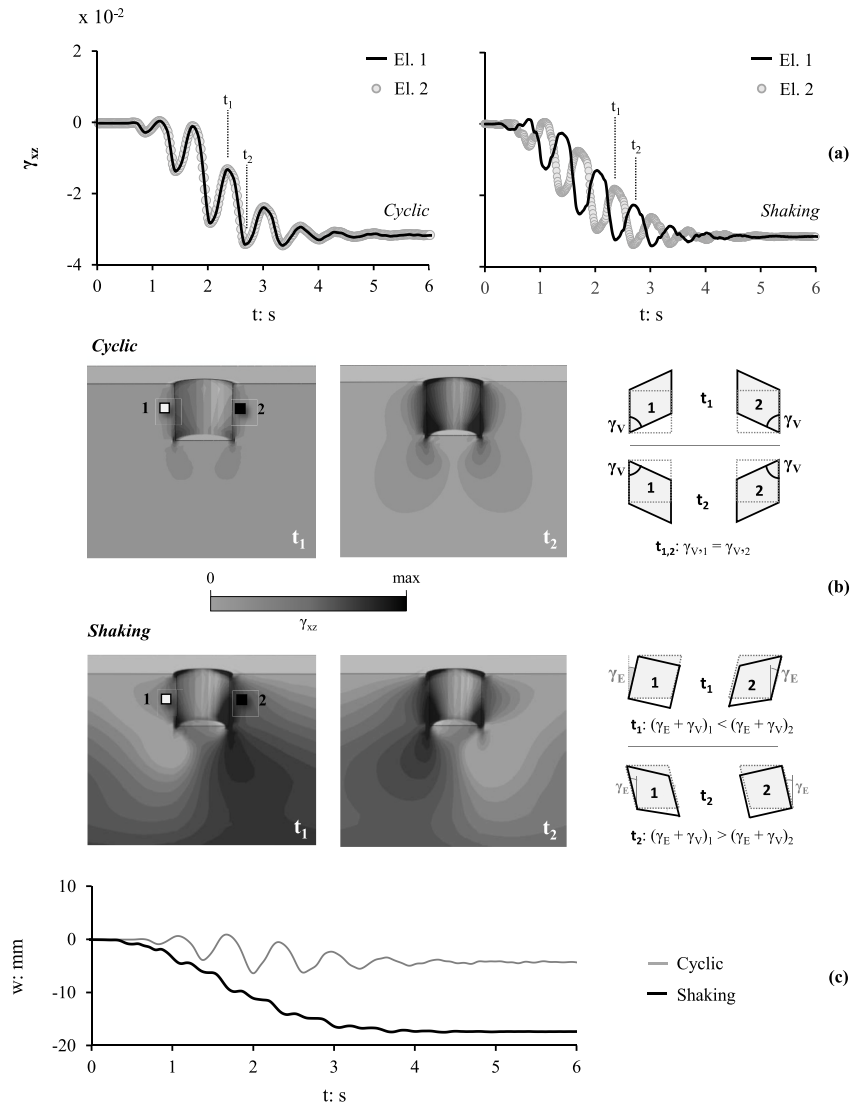


Fig. 11. Investigation of mechanisms controlling seismic response of caissons in clay: (a) the shaking scenario, (b) the cyclic scenario, and (c) comparison of shear stress – shear strain loops at two characteristic soil elements (1 and 2).



**Fig. 12.** Comparison of cyclic loading to seismic shaking scenarios in terms of: (a) shear strain ( $\gamma_{xz}$ ) time histories at two characteristic soil elements (1 and 2); (b) shear strain contours at times  $t_1$  and  $t_2$ , along with schematic illustration of the shearing mechanism at caisson sides; and (c) caisson settlements.

In the shaking scenario, the developing shear strains  $\gamma_{xz}$  are due to the coupled effect of shearing  $\gamma_V$  caused by the vertical static load  $V_w$ , and shearing  $\gamma_E$  due to the vertically propagating shear waves. At  $t = 0$  (initiation of shaking), the two elements display the same shearing due to vertical loading ( $\gamma_{V,1} = \gamma_{V,2}$ ). However, at  $t = t_1$ , the kinematically induced (by the propagating shear waves) shear strain mandates an anti-symmetric deformation pattern (Fig. 12b, bottom): the shear strain of element 1 (left) is reduced, while that of element 2 (right) is increased:  $(\gamma_V + \gamma_E)_1 < (\gamma_V + \gamma_E)_2$ . The opposite pattern is observed at  $t = t_2$ . As a result, the two opposite sides of the caisson (left and right) experience different shear stress at any time  $t$ , as imprinted in the observed phase difference of  $\gamma_{xz}$  (Fig. 12a). This leads to a "rocking" response of the caisson, which leans towards the left or the right during subsequent acceleration cycles, thereby accumulating settlement both for negative and positive loading peaks. As a result, a pronounced difference appears in the accumulated settlement, which reaches  $w = 17$  mm for the shaking scenario, as opposed to  $w = 4$  mm for cyclic loading (Fig. 12c).

Naturally, the rate of settlement accumulation will depend (among other factors) on the specific characteristics of the excitation (i.e., its amplitude and frequency content) and the mean ( $V_w$ ) and maximum value of the bearing load of the caisson  $V_{dyn}$ . These very effects are

further elaborated in Sections 5.2 and 5.3. Section 5.2 demonstrates the effect of the non-constant vertical load on the mechanics of seismic settlement accumulation. Section 5.3 discusses the seismic performance of a single caisson under multiple earthquake records (assuming that all other model parameters remain constant) and investigates the correlation of maximum permanent settlement to characteristic ground motion parameters.

### 5.2. The effect of non-constant $V$

In the previous section, it was tacitly assumed that, simultaneously with the seismic loading (shaking scenario), the caisson is subjected to a constant axial load  $V_w$  that corresponds to the load acting on the windward leg of the jacket due to wind loading ( $W$ ). In reality, however, the axial forces developing on the jacket legs during shaking are not constant. A preliminary set of 3D FE analyses was therefore performed to quantify the effect of non-constant  $V$  on the caisson settlement (Fig. 13). To this end, the settlement computed using the global 3D FE model under combined ( $W+E$ ) loading is compared to the single 3D FE model subjected to the same seismic excitation, but assuming a constant vertical load  $V_w$ . The comparison is performed for medium (L'Aquila, 2009)

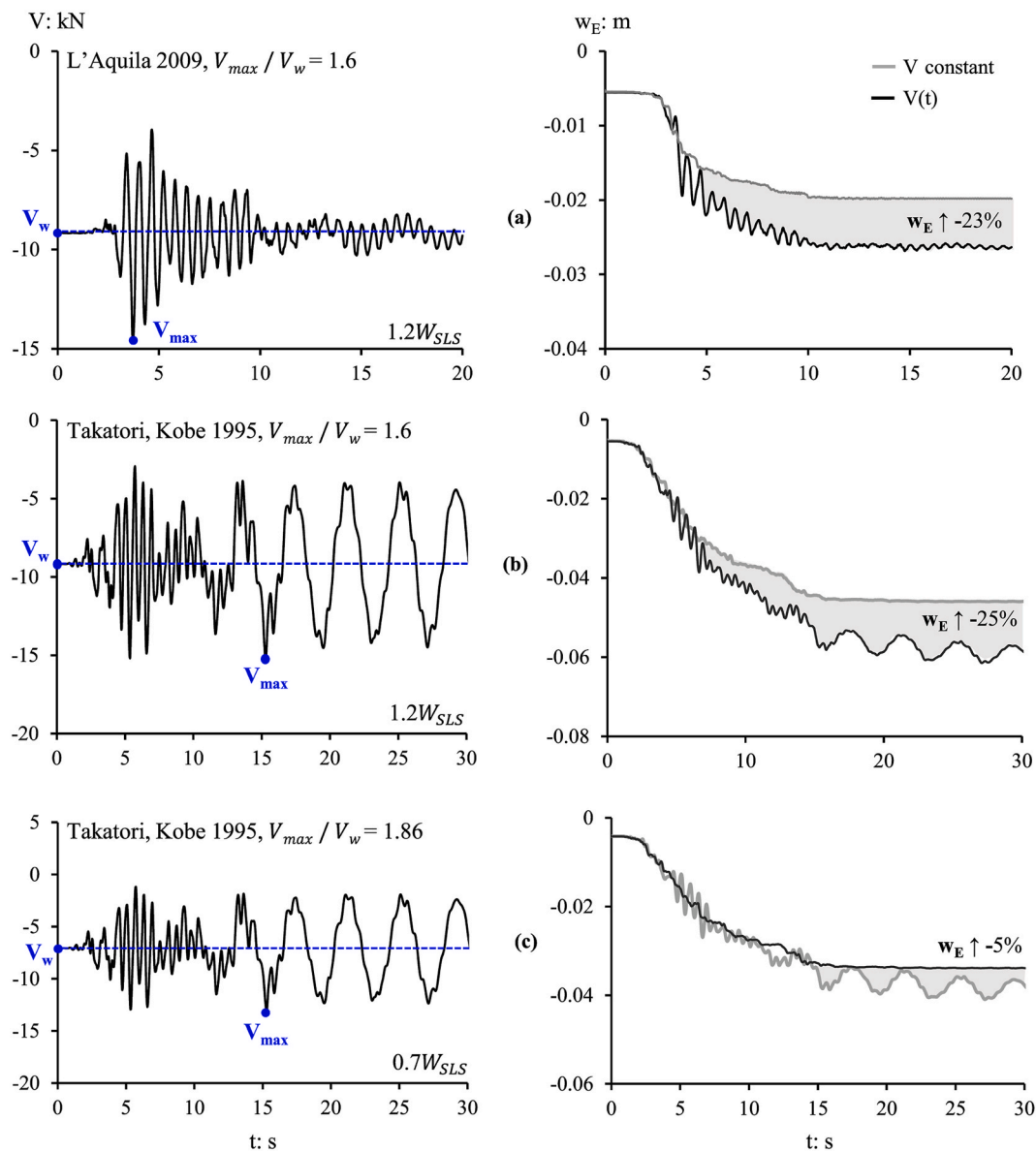


**Fig. 13.** Comparison of settlement time histories ( $w_E$ ) for constant vertical load  $V = V_w$  to those of the global 3D FE model (non – constant  $V$ ): (a) medium intensity shaking (L'Aquila 2009) with  $V_{max}/V_w = 1.6$  ( $0.7 W_{SLS}$ ); (b) large intensity shaking (Takatori, Kobe 1995) with  $V_{max}/V_w = 1.7$  ( $1.2 W_{SLS}$ ); and (c) same excitation, but with  $V_{max}/V_w = 1.86$  ( $0.7 W_{SLS}$ ).

and large intensity shaking (Takatori, Kobe 1995). In Fig. 13a, the results are shown for the L'Aquila record combined with an increased wind thrust  $1.2 W_{SLS}$  (i.e., exceeding SLS by 20%), generating a ratio of maximum seismic axial load to initial vertical load  $V_{max}/V_w = 1.6$  (while  $V_w = 9.16 MN$ ). The assumption of constant vertical load  $V_w$  leads to an appreciable underestimation of the settlement  $w$  by 23%. The same wind load, combined with the stronger Takatori record, yields  $V_{max}/V_w = 1.7$  and to a slight increase of the underestimation of  $w$  by 25% (Fig. 13b). The same seismic excitation (Takatori) combined with a reduced wind load  $0.7 W_{SLS}$  ( $V_w = 7.07 MN$ ), yields an increased  $V_{max}/V_w = 1.86$  and much smaller underestimation of  $w$  by a mere 5% (Fig. 13c). It may therefore be concluded that the underestimation of settlement is mainly related to the value of  $V_w$ , and to a lesser extent to  $V_{max}$ .

### 5.3. The effect of earthquake motion variability

It is generally accepted that the seismic performance (also referred to

as damage potential) of nonlinear systems is strongly dependent on the earthquake excitation's particular characteristics, commonly referred to as Intensity Measures (IMs). To name a few: the frequency content, the maximum acceleration, the duration, the important cycles of the excitation will eventually determine the level of accumulated settlement. As a result, attempting to correlate damage potential with any single IM introduces significant uncertainty [52,53]. Correlations may be improved when combining different IMs. For example, Anastasopoulos et al. [54] and Sakellariadis et al. [55] successfully correlated seismic performance indices of motorway bridges with statistically significant IMs, combining FE simulations with advanced econometric modelling. Similarly, in Marin et al. [56] the correlation between input motions and co-seismic displacements of slopes was shown to be markedly improved by matching the relative significant duration (RSD), the Arias Intensity ( $I_A$ ), and the spectral acceleration (SA) to characterize and select input motions.

Building on these findings, the current study employs a similar deterministic approach based on FE modelling to assess the efficacy of a



double-parameter correlation for the estimation of the seismic settlement of caissons in which the first parameter is a targeted site response spectrum and the second the Arias Intensity. For demonstration purposes, the single 3D FE model is here excited by an ensemble of input motions (derived from real parent accelerograms) that have been pre-processed to match a reference spectrum: the EC8 Type Soil-C design spectrum assuming peak ground acceleration  $PGA = 0.35$  g. An initial static load  $V_w$  is applied to the model prior to seismic shaking. The geometry and material parameters of the single 3D FE model are modified in this section to correspond to an example  $L = D = 4.5$  m caisson, founded on a uniform clay stratum of  $S_u = 75$  kPa and  $E_o = 134.5$  GPa. The computed permanent seismic displacements are plotted against the Arias Intensity ( $I_A$ ) of the respective matched motions to derive a linear correlation.

### 5.3.1. Parent accelerograms

The ensemble of 22 real accelerograms is selected from international ground motion databases (e.g., the PEER Strong Ground Motion Databases<sup>2</sup>). Table 5 summarizes their key characteristics, including the moment magnitude ( $M_w$ ), Peak Ground Acceleration (PGA) and soil type according to EC8. The rationale behind the records' selection is two-fold:

- Ground motions recorded on similar site conditions as the design earthquake were preferred (soil type B or C) to allow compatibility with the spectrum.
- The selected motions are intended to cover a wide range of frequency content (especially in the period range  $T = 0.01$ – $4$  s), to allow for the smooth application of Method B, which requires the median spectrum to fit the target EC8 spectrum without a change in the motions' frequency content.

Two different matching strategies have been implemented to derive spectrum-compatible input motions:

**Method A: One-by-one spectrum matching** (Fig. 14a). Spectrum compatible input motions across the entire range of periods  $T = 0.01$  –  $4$  s are produced, either by generating artificial waveforms based on published intensity envelopes [57–59] or through direct mathematical manipulation of real records in the frequency domain. In the second case, the physical characteristics of the seismic motion (e.g., number of cycles) are retained, rendering the technique more appealing than artificial motion generation. The SeismoMatch software is used to produce the spectrum-compatible records of Method A [60]. The application adjusts accelerograms to match a specific target response spectrum using the algorithm proposed by Al Atik and Abrahamson [61].

**Method B: Median spectrum match** (Fig. 14b). Although Method A is widely used in practice, the motions generated through one-to-one spectrum matching are often criticized for being unrealistic. Since the design spectrum represents an envelope of possible spectral accelerations rather than an actual seismic event, one-to-one spectrum matching leads to a distorted frequency content. For this reason, performance-based assessment methods (e.g., ATC-58) often require a more realistic description of the seismic excitation. This requirement is met by Method B, which aims at matching the response spectrum on average while preserving the frequency content and the physical characteristics of each of the original motions. This may be considered a more natural process, mimicking the way the design spectra have been developed. In this simpler approach, a set of seismic records are scaled one by one only in terms of amplitude, without altering their frequency content. The procedure involves several iterations (performed in Excel VBA environment), where the scaling factors are readjusted until the best fit of the median to the target spectrum is obtained (i.e., the residual between the median and the target spectrum is below a pre-specified limit.). The

**Table 5**

Key characteristics of the selected ground motions.

Record No.	Event	Station	$M_w$	Soil Type	PGA [g]	Method B scaling factor
1	San Salvador, US, 1986	NGI (180)	5.7	C	0.392	1.5
2	Northridge, US, 1994	Jensen (292)	6.7	B	0.424	1.6
3	Kocaeli, Turkey, 1999	Yarimca (060)	7.4	B	0.268	2.0
4	Loma Prieta, US, 1989	Gilroy #2 (000)	6.9	C	0.367	2.0
5	Loma Prieta, US, 1989	Treasure Island (000)	6.9	C	0.0855	4.0
6	San Fernando, California, US, 1971	Pacoima dam (254)	6.6	B	1.160	0.6
7	Tabas, Iran, 1978	Tabas	7.4	B	0.836	0.5
8	Lefkada, Greece, 2003	Lefkada (Long. Dir.)	6.2	C	0.348	1.6
9	Kobe, Japan, 1995	Takatori (000)	6.9	C	0.611	1.0
10	Imperial Valley, El Centro, US, 1940	El Centro (270)	6.9	C	0.215	2.4
11	Erzincan, Turkey, 1992	Erzincan (Station 95)	6.7	C	0.481	0.6
12	Lytle Creek, US, 1970	Wrightwood - 6074 Park	5.3	B	0.143	0.7
13	Northern Calif-03, US, 1954	Ferndale City Hall	6.5	C	0.162	0.7
14	Superstition Hills-02, US, 1987	El Centro Imp. Co cent.	6.5	C	0.340	0.8
15	Whittier Narrows-01, US, 1987	Brea Dam	6.0	B	0.171	0.7
16	Morgan Hill, US, 1984	Anderson Dam	6.2	B	0.416	0.6
17	Irpinia, Italy, 1980	Brienza	6.9	B	0.175	2.0
18	Laquila, Italy, 2009	IT.AC.V	6.3	B	0.657	1.0
19	Friuli 3 <sup>rd</sup> Shock, Italy, 1976	E.FRC	6.5	B	0.332	1.7
20	Emilia-Romagna, Italy, 2012	Mirandola	6.1	C	0.264	1.2
21	ChiChi, Taiwan, 1999	TCU052	7.7	C	0.350	1.2
22	Iquique, Chile, 2014	GO01	8.2	B	0.361	1.2

scaling factors that resulted in the best fit of the median to the target spectrum during the amplitude-based scaling of Method B are tabulated in Table 5.

### 5.3.2. Seismic settlement – $I_A$ correlation

Fig. 15 plots the final seismic caisson settlement ( $w_E$ ) for Method A records against the Arias Intensity  $I_A$  [62], which is defined as:

$$I_A = \frac{\pi}{2g} \int a_{ff}(t)^2 dt \quad (16)$$

where  $a_{ff}(t)$  stands for the acceleration time history at the free field.

It should be clarified that the proposed charts correspond to permanent caisson settlements. The final caisson settlement  $w_E$  utilized for the charts' construction corresponds to the summation of incremental settlements  $Dw$  occurring during consecutive acceleration cycles. Such response is in accordance with the results of Section 5.1, where a single

<sup>2</sup> <https://peer.berkeley.edu/peer-strong-ground-motion-databases>.

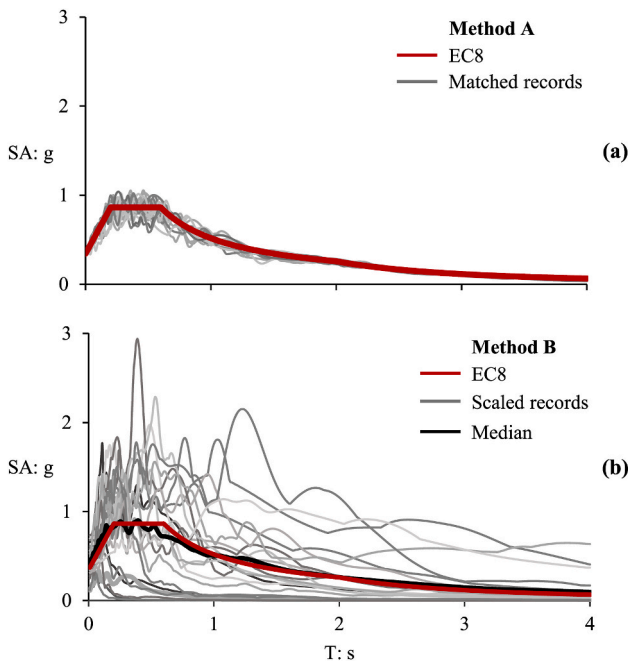


Fig. 14. Records matching the EC8 design acceleration spectrum (Type C) employing two different approaches: (a) Method A, and (b) Method B.

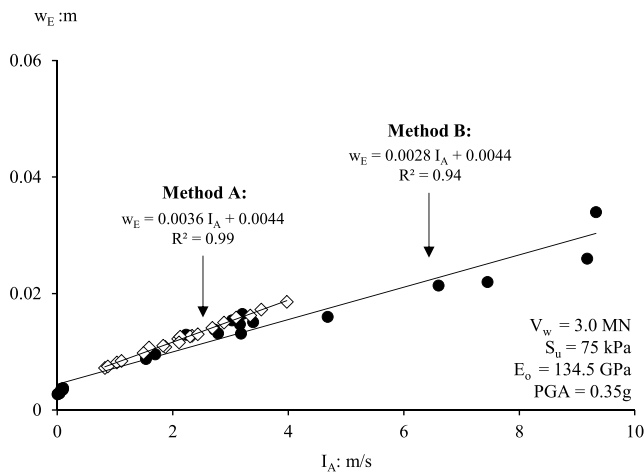


Fig. 15. Correlation of caisson seismic settlement  $w_E$  with the Arias Intensity ( $I_A$ ): comparison of Methods A and B.

caisson is shown to incrementally accumulate inelastic settlements during subsequent cycles of the idealized Tsang-type excitation.

As shown in Fig. 15, for the examined EC8-compatible motions (PGA = 0.35g), the results fit very well a linear equation of the form:

$$w_E = \beta \times I_A + \delta \tag{17}$$

with coefficients  $\beta = 0.0036$  and  $\delta = 0.0044$ . The success of the statistical fit is confirmed by the satisfactory  $R^2 = 0.99$ .

The linearity observed in the derived regression equations is considered valid for the  $w_E - I_A$  range examined herein. The trend is directly correlated with the fact that  $I_A$  is proportional to the integral of the squared acceleration  $a_{ff}(t)$ , meaning that it implicitly incorporates the effect of acceleration amplitude, frequency content, and the number of cycles, which are primarily responsible for the observed accumulation of settlements. Furthermore, the linear trend is also the result of the following:

- The undrained shear strength  $S_u$  and rigidity ratio  $E_o/S_u$  of the clay stratum are constant variables in the examined problem. The resulting expressions would entail a level of nonlinearity in the case of sand materials that experience densification or sensitive clays that experience cyclic degradation phenomena.
- The soil-caisson seismic response is essentially symmetric, i.e., an identical response is expected in both loading directions during the applied seismic SV waves. The derived linear correlations would probably be less successful (i.e., having a lower correlation coefficient) in the case of systems with non-symmetric response, such as retaining walls or slopes.

Data points using Method B are also plotted in the same figure (black dots). It is interesting to note that, although the caisson is subjected here to (22) seismic motions of different PGA, frequency content and number of cycles, the linear correlation between  $w_E$  and  $I_A$  is essentially maintained. A new (not identical, but similar) linear regression equation is derived for Method B ( $\beta = 0.0028$  and  $\delta = 0.0044$ ), yielding  $R^2 = 0.94$ . The statistical correlation is lower than the one of Method A, but the same data points (22 motions) are now spanning over a larger range of  $I_A$ . It is worth observing that for the common range of  $I_A$  (0.1–3 m/s), the two methods yield very similar results, confirming the robustness of the developed prediction equations. The small difference between the two methods suggests that linear regression equations produced with one method can be used to predict the permanent caisson settlement as function of a combination of  $I_A$  and design spectrum, regardless of the employed spectral matching technique (Method A or B).

Figure Fig. 16 offers a close-up of the effect of PGA on the developed linear regression curves. Case 1 in Fig. 16a corresponds to the results of Method A presented in Fig. 15 (for  $PGA = 0.35g$ ). For Case 2, the same analyses were conducted, but with the seismic motions re-manipulated to match the EC8 spectrum with lower  $PGA = 0.24g$ . Interestingly, the derived relation between  $w_E$  and  $I_A$  is insensitive to  $PGA$  (Fig. 16a). This confirms the efficiency of the proposed combination of spectrum matching and  $I_A$  in deriving good correlations with caisson settlement  $w_E$ . Such trend is not present when considering other intensity measures instead of  $I_A$ , such as the Relative Significant Duration ( $RSD$ ). The measure is defined as [72]:

$$RSD = \int_0^{\infty} [H(A_r(t) - 0.05) - H(A_r(t) - 0.95)] dt \tag{18}$$

where:  $H()$  is the Heaviside step function, and  $A_r(t) = I_A(t)/I_{A,max}$ . The  $RSD$  incorporates the effect of motion duration, as it practically indicates the time within which 5–95% of the signal’s energy/intensity is released. Fig. 16b indicates that results are sensitive to different  $PGA$  levels when plotted against the  $RSD$ , while the statistical significance of linear equations is additionally reduced (lower values of  $R^2$  are observed).

## 6. Simplified approach for the preliminary assessment of permanent seismic settlements in SBJ OWTs

The study attempts to generalize the case-specific findings presented in the previous section and propose dimensionless expressions for the preliminary estimation of seismically induced settlements in various suction caissons configurations. To this end, we first employ a formal dimensional analysis of the caissons’ performance in clayey soils to derive families of self-similar problems [63]. Then, for each set of self-similar caisson configurations, we derive a single master line that correlates the Arias Intensity with the dimensional seismically induced settlement of any member of the self-similar family using the methodology of Section 5.3.

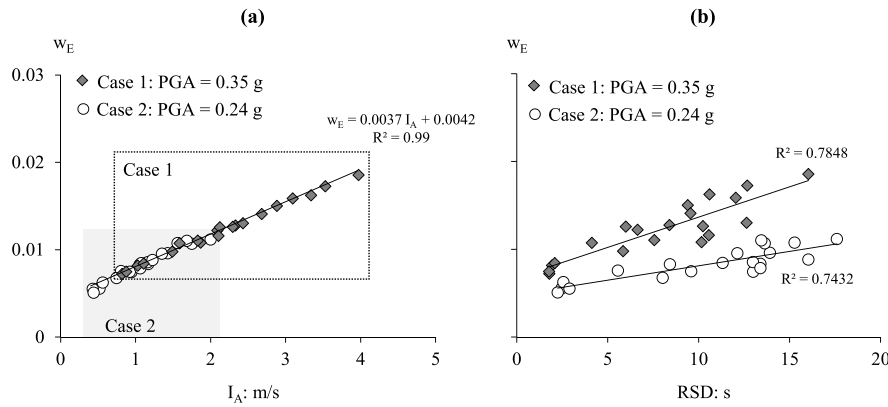


Fig. 16. Correlation of caisson settlement ( $w_E$ ) with (a) the Arias Intensity ( $I_A$ ) and (b) the Relative Significant Duration ( $RSD$ ) using Method A spectrum-compatible seismic motions: The effect of  $PGA$ .

6.1. The dimensional problem

The dimensional analysis employs the single 3D FE model subjected to concurrent axial and seismic loading. Under this loading, the caisson settlement is a function of 8 variables:

$$w_E = f(V_w, D, L, S_u, E_o, \rho, PGA, f_E) \tag{19}$$

where:  $PGA$  and  $f_E$  are the peak ground acceleration and mean frequency of the same, arbitrary shape ground motion. The effect of earthquake motion variability on caisson response is introduced later on, using the derived linear regression equations.

According to the Vaschy-Buckingham  $\Pi$ -theorem of dimensional analysis [64], Eq. 19 can be re-arranged in (8-3) dimensionless  $\Pi$ -products, where 3 is the minimum number of reference dimensions (length, mass, time) necessary for the description of the physical variables:

$$\frac{w_E}{D} = f\left(\frac{V_w}{S_u D^2}, \frac{L}{D}, \frac{E_o}{S_u}, \frac{f_E}{R}, \frac{S_u}{PGA \rho L}\right) \tag{20}$$

where:  $R = \sqrt{E_o / \rho D L}$ .

Parameters  $\frac{E_o}{S_u}$ ,  $\frac{V_w}{S_u D^2}$ ,  $\frac{f_E}{R}$  and  $\frac{S_u}{PGA \rho L}$  are hereafter termed as soil rigidity ratio, vertical capacity ratio, frequency ratio and soil strength mobilization index. A detailed description and validation of the dimensional formulation may be found in [65].

6.2. Response charts

For the derivation of dimensionless settlement charts, the caisson dimensions are varied within a reasonable range for the jacket foundation under consideration, i.e.,  $L = D = 3-9$  m. The examined clay profiles correspond to Soil Type C (i.e., deep deposits of stiff clay with thickness from several tens to many hundreds of meters, according to the EC8 site classification scheme), having undrained shear strength that varies between  $S_u = 70-250$  kPa while the shear wave velocity is within the range of  $V_s = 180-360$  m/s. The FE model is excited with the seismic records of Method A, and aggregated results are plotted in Fig. 17, in the form of linear master lines correlating the dimensionless settlement  $w_E / D$  with Arias Intensity  $I_A$ . Each chart corresponds to a family of self-similar caissons for which the dimensionless variables of Eq. (20) are set equal to predetermined values (that aim to cover a realistic, although not exhaustive, ensemble of possible caisson configurations). Following the discussion of Fig. 16, which demonstrated that spectrum-compatible records of different  $PGA$  may be represented by the same  $w_E / D - I_A$  regression formula, in this set of analyses, the strength mobilization index  $\frac{S_u}{PGA \rho L}$  is replaced by the non-dimensional  $\frac{S_u}{\rho L}$  ratio. It is also clarified

that the charts of Fig. 17 assume a constant vertical load  $V_w$  acting concurrently with seismic loading to represent the wind-induced bearing load on the supports of the jacket. It is therefore advised that the derived dimensionless settlement is multiplied by a factor  $q = 1.1$  to 1.3 (depending on the level of  $V_w / S_u D^2$  and the intensity of seismic shaking) to account for the effect of non-constant  $V_w$  (as discussed in Section 5.2).

For this parametric study, we have assumed constant  $L/D$  and  $E_o/S_u$  ratio, and have parametrically investigated the effect of the remaining three dimensionless variables within the following applicable range:

- $\frac{L}{D}$ , the embedment ratio, is set equal to 1 (which corresponds to the most typical caisson configuration for multi-pod installations)
- $E_o/S_u$ , the soil rigidity ratio, is assumed equally to 1800 (which is a typical rigidity ratio for stiff clay profiles)
- $V_w/S_u D^2$ , the mean vertical capacity ratio, varies between 2.0 and 3.0. The lower vertical capacity ratio is representative of the mean loading of suction caissons under SLS conditions; the higher value is an estimate of the average dimensionless vertical load of the windward caisson near extreme wind, representative of the rare event of an earthquake occurring amidst a storm.
- $\frac{S_u}{\rho L}$  varies between 5.0 and 8.3. The lower bound is representative of soil/caisson systems with reduced soil strength mobilization, i.e., development of larger permanent deformations under the same vertical capacity ratio.
- $\frac{f_E}{R}$  lies within 0.032–0.045 when  $\frac{S_u}{\rho L} = 8.3$  and 0.050–0.058 when  $\frac{S_u}{\rho L} = 5.0$ . This particularly small flexibility of the  $\frac{f_E}{R}$  variable shouldn't be a surprise for such an overconstrained problem. The nominator  $f_E$  (i.e., the mean record frequency) may only slightly vary around a mean value ( $\sim 1.8$  Hz) since the ensemble of applied seismic motions has to conform with the EC8 Type Soil-C design spectrum, and the denominator  $R$  is constrained by the caisson dimensions ( $L = D = 3-9$  m), the minimum acceptable undrained shear strength for a Soil-C profile and the  $\frac{S_u}{\rho L}$  ratio.

The example caisson employed for the analyses of Section 5.3 ( $L = D = 4.5$  m,  $S_u = 75$  kPa,  $E_o = 134.5$  Gpa) corresponds to the lower  $\frac{f_E}{R}$  bound for  $\frac{S_u}{\rho L} = 8.3$ ; its dimensionless response is characterized by Eqs. [i] and [i<sub>a</sub>] in Fig. 17a.

The parameters of all linear regression equations presented in Fig. 17 are tabulated in Table 6, which also includes the mean average percentage error (MAPE) for each equation:

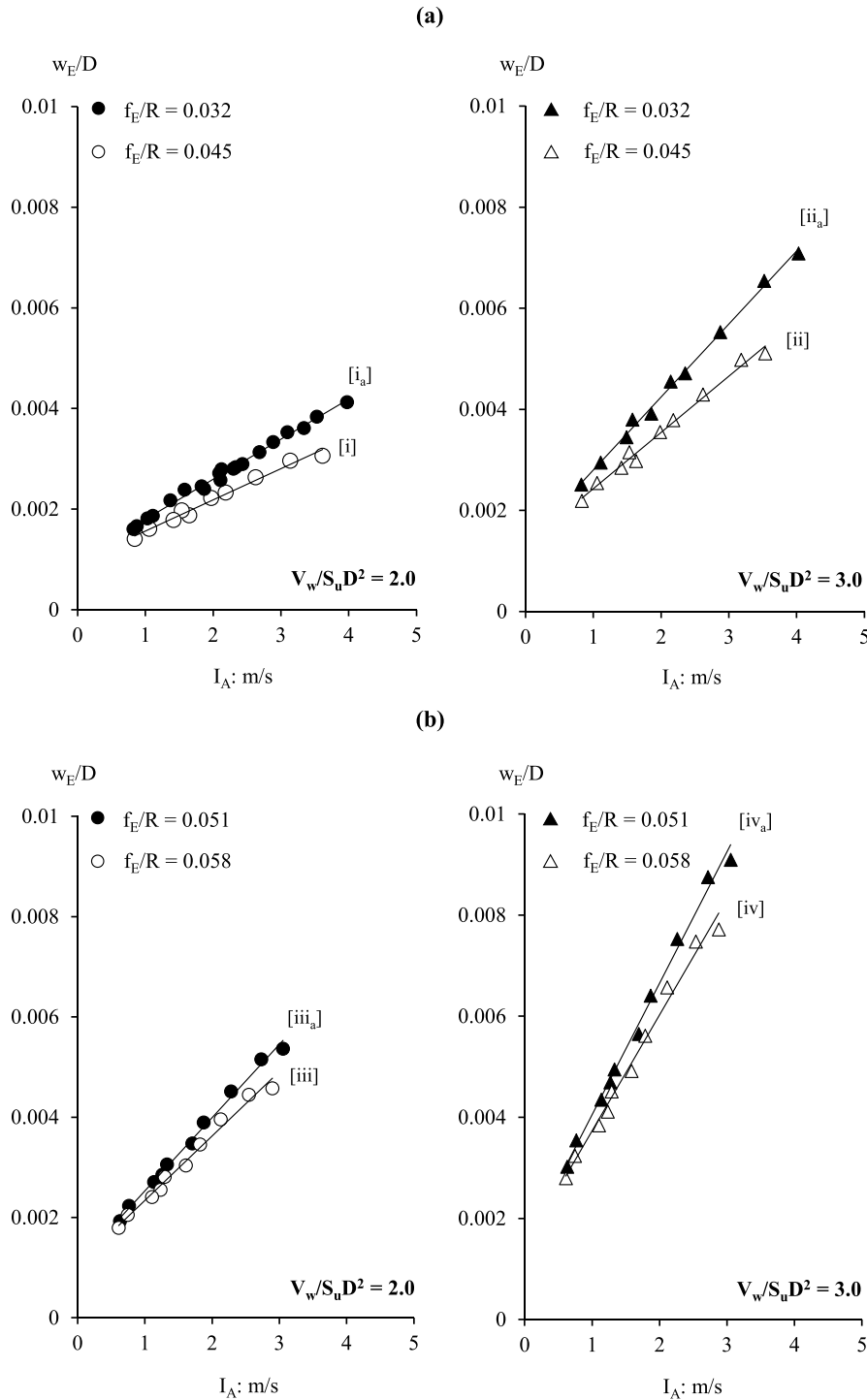


Fig. 17. Dimensionless caisson response charts for Method A and  $E_v/S_u = 1800$ : (a)  $\frac{S_u}{\rho L} = 8.3$ , (b)  $\frac{S_u}{\rho L} = 5.0$ .

$$MAPE = \frac{1}{n} \sum_{i=1}^n |PE_i| \quad (21)$$

where:

$$PE = 100\% \left[ \frac{(w_E/D)_i - (\widehat{w_E/D})_i}{(w_E/D)_i} \right] \quad (22)$$

is the percentage error for observation  $I$  of the predicted with the linear regression equation dimensionless settlement  $(\widehat{w_E/D})_i$ , to the FE-computed dimensionless settlement  $(w_E/D)_i$ . As summarized in

Table 6, the MAPE of the derived regression equations ranges from 1.8% to 3.9%, which is considered a success.

As it should be expected, Fig. 17 indicates that an increase in load ratio  $V_w/S_u D$  leads to the increase of  $w_E/D$  (comparison between Fig. 17a, left and Fig. 17a, right). The same holds true for a decrease in parameter  $\frac{S_u}{\rho L}$ , which indicates lower mobilized soil shear strength. The decrease of frequency ratio  $\frac{f_E}{R}$  also results in slightly augmented dimensionless settlement for the examined systems; however, this difference is diminished in the case of  $\frac{S_u}{\rho L} = 5.0$ , due to the quite narrow  $\frac{f_E}{R}$  band.

**Table 6**  
Parameters of the linear regression equations  $w_E/D$  - $I_A$  presented in Fig.17.

Eq.	PGA [g]	$f_E/R$	$E_o/S_u$	$V_w/S_u D^2$	$R^2$	$\beta$	$\delta$	MAPE (%)
[i]	0.35	0.045	1800	2.0	0.98	0.0006	0.0009	3.9
[ii]	0.35	0.045	1800	3.0	0.99	0.0011	0.0013	2.6
[iii]	0.35	0.058	1800	2.0	0.99	0.0013	0.0011	3.4
[iv]	0.35	0.058	1800	3.0	0.99	0.0023	0.0014	2.9
[i <sub>a</sub> ]	0.35	0.032	1800	2.0	0.99	0.0008	0.001	1.8
[ii <sub>a</sub> ]	0.35	0.032	1800	3.0	0.99	0.0014	0.0014	1.9
[iii <sub>a</sub> ]	0.35	0.051	1800	2.0	0.99	0.0015	0.0011	2.9
[iv <sub>a</sub> ]	0.35	0.051	1800	3.0	0.99	0.0026	0.0015	2.3

### 6.2.1. Implications for foundation design

According to the current state of practice (e.g., [70]), the permanent foundation rotation should not exceed  $0.25^\circ$  (0.0044 rad) for the continuation of operations. For a jacket structure founded on suction caissons, of relevance is the jacket rotation ( $\theta_j$ ), which is generated by the differential settlement between leeward and windward legs. Based on the settlement accumulation patterns presented within the paper, it may be assumed that the windward caisson's residual settlement dominates the jacket rotation. To this end, it is possible to correlate  $\theta_j$  to a threshold settlement at the windward leg, considering zero residual settlements at the leeward leg. The latter comprises a reasonable assumption, considering that the initial settlement of the leeward leg (due to the dead weight of the superstructure) is counterbalanced by the uplift displacement experienced due to the application of wind and seismic loading. For a realistic OWT jacket structure (for the size of the caissons examined herein), this results in a settlement threshold  $w_{lim} = 55$  mm, or  $w_{lim}/D = 0.006$  in dimensionless terms, for a  $D = L = 9$  m caisson. Based on the results of Fig. 17, it may safely be concluded that a single seismic event is hardly ever expected to threaten the operability of a jacket OWT, except for the highly improbable case of a strong earthquake occurring amid a storm for caissons with low  $\frac{S_u}{\rho L}$  ratios (Fig. 17b, right). However, the sustained seismic settlement and the resulting permanent  $\theta_j$  will unavoidably reduce the remaining operational life of the OWT. For example, a seismic event of  $I_A = 3$  m/s may lead to approximately  $w_E/D = 0.0045$  for a caisson with  $\frac{S_u}{\rho L} = 5.0$  under normal environmental loads (Fig.17b, left). Therefore, the remaining threshold for settlement accumulation due to long-term environmental cyclic loading will be significantly diminished:  $w_{rem}/D = w_{lim}/D - w_E/D = 0.006 - 0.0045 = 0.0015$ .

### 6.2.2. Use & limitations of the developed regression equations

It is acknowledged that a different or richer dataset of ground motions may slightly change the constants of the derived regression equations. However, it is not expected to essentially affect the observed linear trends for the examined problem. The methodology is validated across the entire range of common  $I_A$  values, while the selected ground motions incorporate all primary parameters affecting the investigated problem: acceleration amplitude, frequency content, and number of cycles.

The presented linear regression equations should be treated with caution for sites that do not match the environmental and soil parameters, or the foundation configuration examined herein. This includes 4-pod SBJs on a uniform clay stratum founded on  $L/D = 1$  caissons, under a specific range of wind loads (applicable to the examined Mediterranean Sea site, or any similar site in terms of environmental load conditions) and soil rigidity ratios (stiff clays). Moreover, the charts' application is limited to  $S_u/\rho L$  between 5.0 and 8.3, and the associated frequency ratio ( $f_E/R$ ) range.

Despite their undeniable limitations, the value of the response charts lies on the underlying methodological framework rather than the regression equations per se. In this context, the same methodology may be employed with more sophisticated soil constitutive models to derive prediction equations for the same or any other type of caisson

configuration.

## 7. A hybrid approach for the seismic assessment of SBJ OWTs

A hybrid methodology for performance-based seismic assessment of SBJ offshore wind turbines is proposed, combining the nonlinear CWS modelling technique and seismic settlement prediction using the derived linear regression equations. The hybrid methodology comprises eight consecutive steps:

**Step 1.** Define the design acceleration response spectrum (EC8 or equivalent site-specific spectrum).

**Step 2.** Estimate the Aria's intensity ( $I_A$ ) (mean and standard deviation) at the reference site, using regression formulas that correlate  $I_A$  to earthquake magnitude, distance from the fault, and the local soil conditions (e.g., [66–68]).

**Step 3.** Generate an ensemble of spectrum-compatible seismic motions (Method A or B).

**Step 4.** Define the mean environmental loads acting on the OWT (Wind, Wave loads) pertinent to the loading combination ( $W + E$ ), as well as the soil conditions ( $E_o$ ,  $S_u$ ) at the site of reference.

**Step 5.** Subject the global CWS model to pure environmental loading and compute the axial load  $V_w$  and the respective dimensionless term  $V_w/S_u D^2$  at the leeward and windward legs.

The proposed model captures soil-structure interaction (SSI) effects, in contrast with fixed-base superstructure models, or further simplified models where SSI effects are taken into account by replacing the substructure with a set of elastic springs that correspond to the vertical ( $K_V$ ), lateral ( $K_H$ ) and rocking ( $K_R$ ) soil-caisson stiffness. On the cost of accuracy, users may replace the proposed model with a simpler one to compute  $V_w$ .

**Step 6.** Subject the global CWS model to combined environmental and seismic loading (using the motions of Step 3) and compute the horizontal displacement  $u$  and rotation  $\theta$  of individual caissons. Due to the lower model accuracy regarding the calculation of seismically induced deformations, it is advised that results are used for preliminary assessment only.

Step 6 is redundant if the interest lies solely in the estimation of the jacket rotation  $\theta_j$  (i.e., the rotation stemming from the differential settlement of the caissons). In this case, users should directly move to Step 7.

**Step 7.** Use the spectrum-compatible linear regression equations to preliminarily assess the seismic settlement  $w_c$  at the (critical) compressive leg (for the  $V_w/S_u D^2$  calculated in Step 5, the  $E_o/S_u$  ratio that best describes the site conditions and a reasonable range of  $I_A$ , compatible with the seismological profile of the area if interest).

**Step 8.** Estimate the jacket rotation  $\theta_j \approx w_c/B$  and compare against threshold values.



## 8. Conclusions

The paper has developed a simplified performance-based assessment technique for SBJ OWTs founded in clay under the combined action of wind ( $W$ ) and earthquake ( $E$ ) loading. Using an example of an 8 MW jacket-supported OWT, installed at 60 m depth in the Adriatic Sea, system performance was assessed employing a detailed 3D FE model of the soil–foundation–structure (SFS) system (global 3D FE model). After deriving insights on system performance, the global 3D FE model was used as a *benchmark* to assess the efficiency of an enhanced Winkler-based "Caisson-on-Winkler-Soil" (CWS) model. Soil–suction caisson interaction is represented by nonlinear hysteretic elements, capturing residual deformations and hysteresis. The proposed CWS model offers physical coupling between vertical and moment loading by introducing distributed vertical hysteretic elements along the caisson shaft, simultaneously contributing to vertical and moment shaft resistance.

The CWS model was shown to offer a very good prediction of the  $H$ – $M$  failure envelope in the most relevant first quadrant of  $H$ – $M$  space, where the loads are acting in the same direction. It was subsequently employed to predict the response of the Jacket OWT subjected to transient VHM loading, generated by the combined action of a steady wind force and seismic excitation. Subjected to external inertia loading, the CWS model successfully predicted the nonlinear dynamic response of the caisson, matching well with the *benchmark*. The windward caisson's residual settlement was shown to be critical for design, as it controls jacket rotation  $\theta_j$ .

The global CWS model was shown to capture wave propagation effects imposed by the non-uniform free-field deformation pattern. However, when subjected to seismic loading at the base, it was unsuccessful in predicting caisson settlements (horizontal displacements and rotations were less affected). The caisson was shown to be subjected to a *dual shearing* mechanism due to: (i) *kinematic* loading by vertically propagating S-waves; and (ii) *inertial* loading from the superstructure. The simplified CWS model cannot capture such a *dual-shearing mechanism* since the horizontal hysteretic elements are *not coupled* to the vertical ones. This is an inherent limitation of any *uncoupled* analysis.

The 3D FE model of a single caisson (single 3D FE model) was used to shed light on the mechanisms controlling permanent caisson deformations. In stark contrast to cyclic inertia loading, where the caisson accumulates settlement only when subjected to compressive loads, the combination of *kinematic* and *inertia* (coupled) loading leads to an anti-symmetric deformation pattern. The developing shear strains are due to the *coupled* effect of shearing  $\gamma_V$  caused by the initial vertical load  $V_w$ , and shearing  $\gamma_E$  due to the vertically propagating shear waves. While  $\gamma_V$  is constant, the fluctuation of  $\gamma_E$  leads to a "rocking" response, due to which the caisson accumulates settlement both for negative and positive load peaks.

Recognizing the inability of the simplified CWS model to predict seismic settlements realistically, the single 3D FE model was used to develop settlement prediction equations for the critical windward caisson. A methodology is proposed to derive meaningful correlations of co-seismic caisson settlement ( $w_E$ ) with statistically significant Intensity Measures (IMs). Firstly, spectrum compatible input motions are generated, following two alternative strategies: (a) Method A – one-by-one

spectrum matching, manipulating actual records in the frequency domain; and (b) Method B – median spectrum matching, manipulating the records only in amplitude. Then, the spectrum compatible motions were used to conduct a numerical study with the single 3D FE model, the results of which were used to derive linear regression equations, correlating  $w_E$  with  $I_A$ . The efficiency of the method was demonstrated using an example  $L/D = 1$  caisson, subjected to 22 seismic records, scaled to match the EC8-Type C spectrum, using both spectrum-matching techniques. The results were shown to be relatively insensitive to the spectrum-matching technique, with the goodness-of-fit  $R^2$  ranging from 0.94 to 0.99.

A parametric study was then conducted, based on a formal dimensional analysis, which correlated the seismic foundation response with five dimensionless  $\Pi$ -products relevant to the caisson geometry ( $L, D$ ), the soil properties ( $\rho, E_o, S_u$ ), the initial (deadweight + wind) vertical load ( $V_w$ ), and the earthquake characteristics (PGA,  $f_E$ ). The dimensionless permanent caisson settlement ( $w_E/D$ ) was presented as a function of  $I_A$  in the form of response charts, dependent on the derived dimensionless products. The fluctuation of vertical load ( $V_w$ ) during shaking was shown to increase the accumulation of caisson settlements by 10–30% (compared to the assumption of constant ( $V_w$ )). Yet, the increase is primarily dependent on the dimensionless load ratio  $V_w/S_u D^2$  (i.e., the average wind thrust at the onset of the earthquake).

Finally, a hybrid step-by-step method was outlined, facilitating the performance-based seismic assessment of SBJ OWTs. The method employs the simplified CWS model to calculate the VHM loads and approximately estimate horizontal displacements and rotations at the caissons, followed by a preliminary assessment of caisson settlements using the correlations of  $w_E/D$  with  $I_A$ , on the basis of spectrum-compatible input motions.

## Author statement

M. Antoniou: Conceptualization, Methodology, Investigation, Visualization, Writing – original draft, Writing – review & editing. R. Kourkoulis: Conceptualization, Methodology, Visualization, Writing – review & editing, Project administration, Funding acquisition. F. Gelagoti: Conceptualization, Methodology, Visualization, Writing – review & editing. I. Anastasopoulos: Conceptualization, Methodology, Writing – review & editing, Supervision.

## Declaration of competing interest

The authors declare that they have no known competing financial interests or personal relationships that could have appeared to influence the work reported in this paper.

## Acknowledgement

This research has received funding from the Hellenic Foundation for Research and Innovation and the General Secretariat for Research and Technology (GSRT) under grant agreement no. 974.

## Appendix A

The geometric details of the jacket structure supporting the examined 8 MW turbine are illustrated in [Figure A1](#) and [Table A1](#) [36].and.



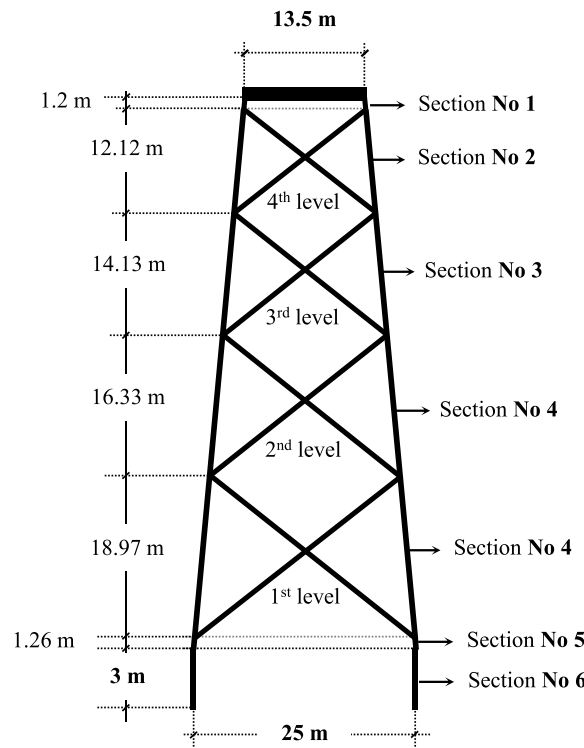


Fig. A1. Geometric properties of the examined jacket structure.

Table A1  
Section properties of the examined jacket structure.

	Braces				Main tubulars					
	1 <sup>st</sup> level	2nd level	3 <sup>rd</sup> level	4th level	Section No 1	Section No 2	Section No 3	Section No 4	Section No 5	Section No 6
D: mm	965	813	711	610	1525	1525	1525	1525	1525	1525
t: mm	21	21	21	21	51	30	35	40	83	45

References

[1] WindEurope. Wind energy in Europe in 2019 - trends and statistics. Technical Report. February 2020. 2020.

[2] Seidel M. Jacket substructures for the REpower 5M wind turbine. Berlin, Germany: European Offshore Wind Conference and Exhibition; 2007. Dec. 4–6, 2007.

[3] Wagner H, Baack C, Eickelkamp T, Epe A, Lohmann J, Troy S. Life cycle assessment of the offshore wind farm alpha ventus. *Energy* 2011;36(5):2459–64.

[4] Schaumann P, Böker C. Can tripods and jackets compete with monopiles? Copenhagen, Denmark: Contribution to Copenhagen Offshore Wind; 2005. Oct. 26–28, 2005.

[5] Katsanos EI, Thöns S, Georgakis CT. Wind turbines and seismic hazard: a state-of-the-art review. *Wind Energy* 2016;19(11):2113–33.

[6] Swiss Re. Wind farms: harvesting energy on shaky grounds and in stormy seas. Swiss Reinsurance Institute; 2017. Report.

[7] Kaynia AM. Seismic considerations in design of offshore wind turbines. *Soil Dynam Earthq Eng* 2019;124:399–407.

[8] Mardfekri M, Gardoni P. Probabilistic demand models and fragility estimates for offshore wind turbine support structures. *Eng Struct* 2013;52:478–87.

[9] Kim DH, Lee SG, Lee IK. Seismic fragility analysis of 5 MW offshore wind turbine. *Renew Energy* 2014;65:250–6.

[10] Anastasopoulos I, Theofilou M. Hybrid foundation for offshore wind turbines: environmental and seismic loading. *Soil Dynam Earthq Eng* 2016;80:192–209.

[11] Mo R, Kang H, Li M, Zhao X. Seismic fragility analysis of monopile offshore wind turbines under different operational conditions. *Energies* 2017;10(7):1037.

[12] De Risi R, Bhattacharya S, Goda K. Seismic performance assessment of monopile-supported offshore wind turbines using unscaled natural earthquake records. *Soil Dynam Earthq Eng* 2018;109:154–72.

[13] Alati N, Failla G, Arena F. Seismic analysis of offshore wind turbines on bottom-fixed support structures. *Phil Trans Math Phys Eng Sci* 2015;373(2035):20140086.

[14] Zheng XY, Li H, Rong W, Li W. Joint earthquake and wave action on the monopile wind turbine foundation: an experimental study. *Mar Struct* 2015;44:125–41.

[15] Wang W, Gao Z, Li X, Moan T. Model test and numerical analysis of a multi-pile offshore wind turbine under seismic, wind, wave, and current loads. *J Offshore Mech Arctic Eng* 2017;139(3).

[16] Gelagoti F, Georgiou I, Kourkoulis R, Gazetas G. Nonlinear lateral stiffness and bearing capacity of suction caissons for offshore wind-turbines. *Ocean Eng* 2018;170:445–65.

[17] Bransby MF, Yun G. The undrained capacity of skirted strip foundations under combined loading. *Geotechnique* 2009;59(2):115–25.

[18] Byrne BW, Housby GT. Experimental investigations of the response of suction caissons to transient combined loading. *J Geotech Geoenviron Eng* 2004;130(3):240–53.

[19] Gourvenec S, Barnett S. Undrained failure envelope for skirted foundations under general loading. *Geotechnique* 2011;261(3):263–70.

[20] Vulpe C. Design method for the undrained capacity of skirted circular foundations under combined loading: effect of deformable soil plug. *Geotechnique* 2015;65(8):669–83.

[21] Keawsawasvong S, Ukritchon B. Finite element limit analysis of pull-out capacity of planar caissons in clay. *Comput Geotech* 2016;75:12–7.

[22] Mana DSK, Gourvenec S, Randolph M, Hossain MS. Failure mechanisms of skirted foundations in uplift and compression. *Int J Phys Model Geotech* 2012;12(2):47–62.

[23] Ukritchon B, Keawsawasvong S. Undrained pull-out capacity of cylindrical suction caissons by finite element limit analysis. *Comput Geotech* 2016;80:301–11.

[24] Ukritchon B, Wongtoythong P, Keawsawasvong S. New design equation for undrained pull-out capacity of suction caissons considering combined effects of

- caisson aspect ratio, adhesion factor at interface, and linearly increasing strength. *Appl Ocean Res* 2018;75:1–14.
- [25] Suryasentana SK, Byrne BW, Burd HJ, Shonberg A. An elastoplastic 1D Winkler model for suction caisson foundations under combined loading. *Numerical Methods in Geotechnical Engineering IX*, vol. 2. In: Proceedings of the 9th European conference on numerical methods in geotechnical engineering (NUMGE 2018). Portugal: CRC Press; 2018. p. 973. June 25–27, 2018, Porto.
- [26] Skau KS, Grimstad G, Page AM, Eiksund GR, Jostad HP. A macro-element for integrated time domain analyses representing bucket foundations for offshore wind turbines. *Mar Struct* 2018;59:158–78.
- [27] Skau KS, Jostad HP, Eiksund G, Sturm H. Modelling of soil-structure-interaction for flexible caissons for offshore wind turbines. *Ocean Eng* 2019;171:273–85.
- [28] Wang X, Yang X, Zeng X. Seismic centrifuge modelling of suction bucket foundation for offshore wind turbine. *Renew Energy* 2017;114.
- [29] Gerolymos N, Gazetas G. Nonlinear lateral response of caisson foundations. In: Proceedings of the 1st Greece-Japan Workshop on seismic design. Athens, Greece: Observation. Retrofit of Foundations; 2005. p. 125.
- [30] Anastasopoulos I, Gelagoti F, Kourkoulis R, Gazetas G. Simplified constitutive model for simulation of cyclic response of shallow foundations: validation against laboratory tests. *J. Geotech. Geoenviron. Eng., ASCE* 2011;137(12):1154–68.
- [31] Vucetic M, Dobry R. Effect of soil plasticity on cyclic response. *J. Geotech. Eng.* 1991;117(1):89–107.
- [32] Giannakos S, Gerolymos N, Gazetas G. Cyclic lateral response of piles in dry sand: finite element modeling and validation. *Comput Geotech* 2012;44:116–31.
- [33] Hung LC, Kim SR. Evaluation of vertical and horizontal bearing capacities of bucket foundations in clay. *Ocean Eng* 2012;52:75–82.
- [34] Fu D, Gaudin C, Tian Y, Cassidy MJ, Bienen B. Uniaxial capacities of skirted circular foundations in clay. *J Geotech Geoenviron Eng* 2017;143(7).
- [35] Mavrakos S. Med-ocean data and hydrodynamic loading for the North sea and the Mediterranean Sea location, 1.1. Deliverable: JABACO Development of Modular Steel Jacket for Offshore Windfarms; 2016.
- [36] Von Borstel T, Vobeck M. Preliminary design of reference offshore steel jackets for 8MW and 10MW wind turbines. JABACO Development of Modular Steel Jacket for Offshore Windfarms; 2016. Deliverable 1.3.
- [37] Novak M, Aboul-Ella F, Nogami T. Dynamic soil reactions for plane strain case. *J Eng Mech Div* 1978;104(4):953–9.
- [38] Randolph MF, Wroth CP. Analysis of deformation of vertically loaded piles. *J. Geotech. Engng ASCE* 1978;104(12):1465–88.
- [39] O'Rourke MJ, Dobry R. Spring and dashpot coefficients for machine foundations on piles, vol. 78. Special Publication; 1982. p. 177–98.
- [40] Pender MJ. Aseismic pile foundation design analysis. *Bull N Z Soc Earthq Eng* 1993;26(1):49. 160.
- [41] Guo WD. Vertically loaded single piles in Gibson soil. *J Geotech Geoenviron Eng* 2000;126(2):189–93.
- [42] API. API recommended practice 2A-WSD - planning, designing, and constructing fixed offshore platforms. American Petroleum Institute; 2010.
- [43] Anoyatis G, Mylonakis G. Dynamic Winkler modulus for axially loaded piles. *Geotechnique* 2012;62(6):521–36.
- [44] Gerolymos N, Gazetas G. Development of Winkler model for static and dynamic response of caisson foundations with soil and interface nonlinearities. *Soil Dynam Earthq Eng* 2006;26(5):363–76.
- [45] Gerolymos N, Gazetas G. Static and dynamic response of massive caisson foundations with soil and interface nonlinearities—validation and results. *Soil Dynam Earthq Eng* 2006;26(5):377–94.
- [46] Gerolymos N, Gazetas G. Winkler model for lateral response of rigid caisson foundations in linear soil. *Soil Dynam Earthq Eng* 2006;26(5):347–61.
- [47] Assimaki D, Gazetas G. A simplified model for lateral response of large diameter caisson foundations—linear elastic formulation. *Soil Dynam Earthq Eng* 2009;29(2):268–91.
- [48] Tsigginos C, Gerolymos N, Assimaki D, Gazetas G. Seismic response of bridge pier on rigid caisson foundation in soil stratum. *Earthq Eng Vib* 2008;7(1):33.
- [49] Gazetas G. Formulas and charts for impedances of surface and embedded foundations. *J. Geotech. Eng., ASCE* 1991;117(9):1129–41.
- [50] Gazetas G, Dobry R, Tassoulas JL. Vertical response of arbitrarily shaped embedded foundations. *J. Geotech. Eng.* 1985;111(6):750–71.
- [51] Yun G, Bransby MF. The horizontal-moment capacity of embedded foundations in undrained soil. *Can Geotech J* 2007;44(4):409–24.
- [52] Padgett JE, Nielson BG, DesRoches R. Selection of optimal intensity measures in probabilistic seismic demand models of highway bridge portfolios. *Earthq Eng Struct Dynam* 2008;37(5):711–25.
- [53] Garini E, Gazetas G. Damage potential of near-fault records: sliding displacement against conventional "Intensity Measures". *Bull Earthq Eng* 2013;11(2):455–80.
- [54] Anastasopoulos I, Anastasopoulos PC, Agalianos A, Sakellariadis L. Simple method for real-time seismic damage assessment of bridges. *Soil Dynam Earthq Eng* 2015; 78:201–12.
- [55] Sakellariadis L, Agalianos A, Anastasopoulos I. Simplified method for real-time seismic damage assessment of motorway bridges: transverse direction — accounting for abutment stoppers. *Earthq Eng Struct Dynam* 2018;47(6): 1496–521.
- [56] Marin A, Truffer PL, Anastasopoulos I. Combined-intensity-measures matching approach for improved performance-based design of slopes. *Soil Dynam Earthq Eng* 2019;126:105763.
- [57] Hou S. Earthquake simulation models and their applications. *Research Report R68-17*. Cambridge, Massachusetts: Dept. of Civil Eng. Massachusetts Institute of Technology; 1968.
- [58] Liu SC. Autocorrelation and power spectral density functions of the Parkfield earthquake of June 27, 1966. *Bull Seismol Soc Am* 1969;59(4):1475–93.
- [59] Saragoni G, Hart GC. Simulation of artificial earthquakes. *Earthq Eng Struct Dynam* 1973;2(3):249–67.
- [60] Seisimosoft. SeismoMatch - a computer program for spectrum matching of earthquake records. Available from URL: [www.seisimosoft.com](http://www.seisimosoft.com); 2020.
- [61] Al Atik L, Abrahamson N. An improved method for nonstationary spectral matching. *Earthq Spectra* 2010;26(3):601–17.
- [62] Arias A. In: Hansen RJ, editor. A measure of earthquake intensity. Cambridge: MIT Press; 1970. p. 438–83.
- [63] Makris N, Black CJ. Dimensional analysis of rigid-plastic and elastoplastic structures under pulse-type excitations. *J Eng Mech* 2004;130(9):1006–18.
- [64] Buckingham E. On physically similar systems; illustrations of the use of dimensional equations. *Phys Rev* 1914;4(4):345.
- [65] Antoniou M, Gelagoti F, Kourkoulis R, Georgiou I, Karamanos SA. Seismic response of jacket wind-turbines: dimensional analysis of foundations and SSL. In: *Proceedings of the 2<sup>nd</sup> international Conference on natural hazards & infrastructure (ICONHIC2019)*; 2019. June 2019, Crete, Greece.
- [66] Peláez JA, Delgado J, Casado CL. A preliminary probabilistic seismic hazard assessment in terms of Arias intensity in southeastern Spain. *Eng Geol* 2005;77(1–2):139–51.
- [67] Lee CT, Hsieh BS, Sung CH, Lin PS. Regional Arias intensity attenuation relationship for Taiwan considering  $V_{s30}$ . *Bull Seismol Soc Am* 2012;102(1): 129–42.
- [68] Chousianitis K, Del Gaudio V, Kalogeras I, Ganas A. Predictive model of Arias intensity and Newmark displacement for regional scale evaluation of earthquake-induced landslide hazard in Greece. *Soil Dynam Earthq Eng* 2014;65:11–29.
- [70] Det Norske Veritas. Offshore standard DNV-OS-j101, design of offshore wind turbine structures. Høvik: Det Norske Veritas; 2014.
- [72] Trifunac MD, Brady AG. A study on the duration of strong earthquake ground motion. *Bull Seismol Soc Am* 1975;65(3):581–626.
- [73] Esfeh PK, Kaynia M A. Earthquake response of monopiles and caissons for Offshore Wind Turbines founded in liquefiable soil. *Soil Dynam. Earthq. Eng.* 2020;136. 106213.
- [74] Kourkoulis S R, Lekkakis C P, Gelagoti M F, Kaynia M A. Suction caisson foundations for offshore wind turbines subjected to wave and earthquake loading: effect of soil–foundation interface. *Geotechnique* 2014;64(3):171–85.
- [75] Abaqus. Abaqus V 6.13. Providence, RI, USA.: Dassault Systèmes Simulia Corp.; 2013.